Title

High-Rate Lithium Cycling and Structure Evolution in Mo_4O_{11}

Journal

Chemistry of Materials, 34(9)

ISSN

0897-4756 1520-5002

Authors

Vincent, Rebecca C
Luo, Yunkai
Andrews, Jessica L
et al.

Publication Date

2022-04-18

DOI

10.1021/acs.chemmater.2c00420

Peer reviewed

High-Rate Lithium Cycling and Structure Evolution in Mo_4O_{11}

Rebecca C. Vincent,[†] Yunkai Luo,[‡] Jessica L. Andrews,[¶] Arava Zohar,[†] Yucheng Zhou,[§] Qizhang Yan,[∥] Eve M. Mozur,[†] Molleigh B. Preefer,[⊥] Johanna Nelson Weker,[⊥] Anthony K. Cheetham,[†] Jian Luo,[∥,#] Laurent Pilon,[§] Brent C. Melot,[¶,@] Bruce Dunn,[‡] and Ram Seshadri*[,†]

†*Materials Department and Materials Research Laboratory*
University of California, Santa Barbara, California 93106, United States
‡*Department of Materials Science and Engineering*
University of California, Los Angeles, California 90095, United States
¶*Department of Chemistry*
University of Southern California, Los Angeles, California 90089, United States
§*Mechanical and Aerospace Engineering Department*
University of California, Los Angeles, California 90095, United States
∥*Department of Nanoengineering*
University of California San Diego, La Jolla, California 92093, United States
⊥*Stanford Synchrotron Radiation Lightsource, SLAC National Accelerator Laboratory*
Menlo Park, California 94025, USA
#*Program of Materials Science and Engineering*
University of California San Diego, La Jolla, California 92093, United States
@*Department of Chemical Engineering and Materials Science, University of Southern California, Los Angeles, CA 90089, USA*

E-mail: seshadri@mrl.ucsb.edu

Abstract

Shear-phase early transition metal oxides, mostly of Nb, and comprising edge- and corner-shared metal–oxygen octahedra have seen a resurgence in recent years as fast-charging, low-voltage electrodes for Li^+–ion batteries. Mo oxides, broadly, have been less well studied as fast-charging electrodes. Here we examine a reduced Mo oxide, Mo_4O_{11}, that has a structure comprising only corner-connected MoO_4 tetrahedra and MoO_6 octahedra. We show that an electrode formed using micron-sized particles of Mo_4O_{11} as the active material can function as a high-rate Li^+–ion electrode against Li metal, with a stable capacity of over 200 mAh g^{-1} at the high rate of $5C$. *Operando* X-ray diffraction (XRD), entropic potential measurements, and *ex situ* Raman spectroscopy are employed to understand the nature of charge storage. The crystal structure dramatically changes upon the first lithiation, and subsequent cycling is completely reversible with low capacity fade. It is the newly formed, and potentially more layered structure that demonstrates high-rate cycling and small voltage polarization. A space group and unit cell for the new structure is proposed. This finding expands the scope of candidate high-rate electrode materials to those beyond the expected Nb-containing shear-phase oxide materials.

Introduction

With transportation being the largest contributor of greenhouse gas emissions in the U.S.,[1] a large scale switch to electric vehicles (EVs) powered by Li^+–ion batteries and charged from renewable sources could potentially reduce emissions by up to 29%.[1] However, it is unlikely that consumers will switch *en masse* to EVs until the vehicles possess the range and the ability to charge quickly in a manner that is on par with internal combustion engine vehicles. There is thus a great need for Li^+–ion battery electrodes that charge and discharge rapidly.[2] Fast-charging electrode materials with large energy density must possess the ability to transport ions and electrons rapidly.

Shear-phase oxides contain regions of edge-sharing and corner-sharing transition metal octahedra,[3] which promote electronic and ionic conductivity respectively[4] and have emerged as promising high-rate Li^+–ion battery electrode materials.[5–13] Nearly all of these oxides are Nb-based, and since Nb^{5+}, Nb^{4+}, and Nb^{3+} are all accessible oxidation states, they are capable of multielectron redox and therefore high capacities. The voltage associated with these couples (on average 1.5 V *vs.* Li/Li^+) is suitably in the regime expected for anodes. Additionally, since all of the oxidation states of Nb are compatible with octahedral coordination, structural changes with varying oxidation states are somewhat minimal, allowing for stable cycling.

The related Mo oxides have been largely unexplored since the 1980s, although compositions between MoO_3 and MoO_2 have vast structural diversity and could also be quite promising in the realm of fast-charging electrodes.[14] For example, Mo_8O_{23} and Mo_9O_{26} are Magnéli phases displaying crystallographic shear wherein hypothetical ReO_3–structured MoO_3 accommodates oxygen removal by sharing octahedral features and transforming from a completely corner-connected structure to a structure that has edge– and corner–connected octahedra. In Magnéli phases, the shear is along a single direction,[15] in contrast to, for example, block structures. Multielectron redox is expected in Mo oxides, given that Mo^{6+}, Mo^{5+}, and Mo^{4+} are all stable oxidation states. However, the literature on the use

of Mo oxides as electrode materials, particularly fast-charging ones, is somewhat limited.

MoO_2 was an early candidate for a safer Li^+–ion battery anode alternative to metallic lithium,[16,17] and remains of interest for its very low bulk electrical resistivity. However, it has been shown to have poor rate performance attributed to sluggish Li diffusion kinetics.[18] Older electrochemistry studies are inconsistent about staying above the storage voltages of carbon when using carbon-composite electrodes;[19,20] however, even the experiments performed above this voltage demonstrated that the capacity of MoO_2 fades over time, potentially due to dissolution of MoO_2 into the carbonate-based electrolyte.[21]

Consistent with it being a band insulator, α-MoO_3 has lower electronic conductivity than MoO_2.[22,23] However, electrochemical cycling has been demonstrated following the addition of graphite to the electrode.[24,25] The rate performance and other electrochemical properties were significantly improved upon nanosizing the material,[26–29] though the capacity still faded significantly over 100 cycles.[26] The efficacy of nanosized MoO_3[30] and nanosized MoO_{3-x}[31] has been demonstrated for high-rate pseudocapacitive energy storage, along with an analysis of variable-rate cyclic voltammetry (CV) indicative of a combination of bulk redox and surface charge storage, the latter supported by the box-like characteristics of the CV. Nanosizing the active material is often not cost effective on an industrial scale, and materials with greater inherent conductivity are still needed so that nanosizing is not necessary to achieve high-rate cycling.

Reduced Mo oxides (often referred to as "non-stoichiometric" oxides in the literature) with O:Mo ratios between 3 and 2, i.e., between MoO_3 and MoO_2, may offer the desired increase in conductivity.[32] Some reduced Mo oxide phases are metastable, like Mo_5O_{14},[33,34] but orthorhombic Mo_4O_{11} (sometimes called γ-Mo oxide) is known to be the most stable oxide between MoO_3 and MoO_2.[35] A representation of the crystal structure of Mo_4O_{11}, a bronze-related phase,[36] is shown in Figure 1. The structure was originally determined by Magnéli,[37] with the correct space group assigned in later studies.[38,39] This structure can be described by the ordered removal of oxygen from an ReO_3-type structure.[38,40,41] The high

occurrence of MoO_4 tetrahedra is significantly different from other Mo oxides. In contrast with shear phases, this fully corner-connected structure accommodates the oxygen deficiency (referenced to MoO_3) by having a combination of octahedral MoO_6 and tetrahedral MoO_4.[37] This means that, despite being described by the formula Mo_nO_{3n-1}, Mo_4O_{11} is not a Magnéli phase. As a result, Mo_4O_{11} has a more open structure compared to other Mo oxides,[37] which could favor Li^+–ion diffusion and enable fast cycling. Furthermore, electronic structure calculations have suggested that Mo_4O_{11} possesses electronically populated states within a relatively broad band, indicative of electronic conductivity despite the lack of edge-sharing features.[40]

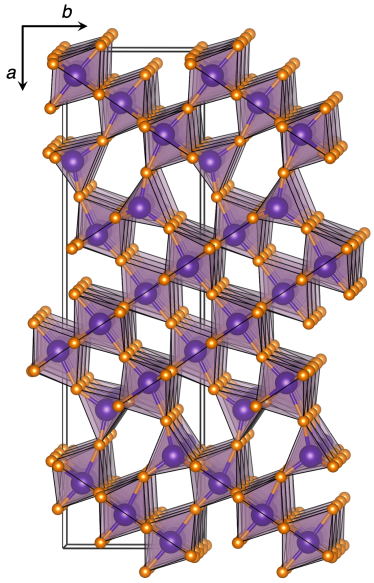

Figure 1: The unit cell of Mo_4O_{11} projected almost down the c axis, structure from refinement of synchrotron data. Mixed-oxidation Mo atoms sit inside octahedra and tetrahedra of oxygen atoms. Crystal structure depicted using VESTA.[42]

There has been some previously reported electrochemical testing of Mo_4O_{11}. The earliest study known to the authors used Mo_4O_{11} with no conductive additives as the cathode in a Li-metal button cell and slowly discharged the cell, intercalating Li into the Mo_4O_{11}.[33] They extrapolated to zero current on a plot of capacity versus discharge current and thus estimated that 2.1 e^- could be transferred per Mo atom in the structure, which would mean multielectron redox and therefore high-capacity.[33] In part II of the same study, the authors

attempted to recharge the cells.[43] The structures were found to change irreversibly with the addition of too much Li, which they said negatively impacted the observed recharge efficiencies.[43] However, the recharge efficiency between the first discharge and charge is not always a good indication of how reversible further cycling will be. In 1980, a study to evaluate the longer-term cycling of Mo_4O_{11} demonstrated multielectron redox, but with almost 50 % capacity fade by the 20th cycle.[34] More recently, approximately 1.88 Li were inserted per Mo when orthorhombic Mo_4O_{11} was discharged to 1.2 V; however, further cycling went down to 0.5 V, a voltage range at which an unfavorable conversion reaction is expected.[44] Likely as a result, significant capacity fade was observed in this voltage range. Given all of these disparate results, it is of interest to revisit the electrochemical properties of Mo_4O_{11} using updated electrochemical techniques, modern cell configurations, and an optimized voltage window.

Here we report the synthesis and electrochemical characterization of orthorhombic Mo_4O_{11}. The compound Mo_4O_{11} can be considered to comprise three $Mo^{6+}O_3$ and one $Mo^{4+}O_2$. Mo^{6+} can be reduced reversibly to Mo^{4+} in the selected voltage range, so on this basis, 6 electrons (along with the corresponding Li^+ ions) can, in principle, be incorporated. The theoretical capacity of Mo_4O_{11} is 288 mAh g^{-1}, corresponding to the insertion of 6 Li according to Equation 1.

$$Mo_4O_{11}(3Mo^{VI}O_3 + Mo^{IV}O_2) + 6Li^+ \rightleftharpoons Li_6Mo_4^{IV}O_{11} \quad (1)$$

We found that the theoretical capacity was exceeded after one galvanostatic discharge to 1.2 V, and after the first discharge the cycling was reversible between 1.2 V and 3.0 V, but the original structure was not retained. A much higher and more reversible capacity was demonstrated for Mo_4O_{11} than in prior studies,[34,44] perhaps due to the optimized cell design and voltage window. When charged up to 3.7 V, the capacity faded much more quickly, which was likely associated with dissolution of the active material into the electrolyte at higher voltages. Micron-sized Mo_4O_{11} particles showed impressive rate capability even

though Mo_4O_{11} is not a shear-structured material and only has corner sharing (of octahedra and tetrahedra) in the structure. *Operando* XRD, *ex situ* Raman studies, transmission electron microscopy (TEM), and entropic potential measurements suggest that the original structure of the material changed irreversibly, and a new structure was then retained reversibly through subsequent cycling. The precise structure of the cycling material is an open question at this time. However, evidence suggests that the structure becomes more layered, and a space group and unit cell parameters that are consistent with the known information are proposed.

Experimental Methods

Solid-state preparation of Mo_4O_{11} To obtain dehydrated MoO_3, a precursor in the synthesis of Mo_4O_{11}, ammonium molybdate (Fisher Scientific) was placed in an alumina crucible and calcined for 10 to 12 hours in a box furnace at 750 °C, then ground in an agate mortar and pestle and put back in the furnace at 750 °C for another 10 to 12 hours. The XRD fit of the dehydrated MoO_3 is given in the Supporting Information (SI), Figure S1. MoO_3 stored in the laboratory outside of a desiccator was found to have absorbed a significant amount of water. Many structures for MoO_3 reported on the Inorganic Crystal Structure Database also give the hydrated structure in which each Mo atom sits in a tetrahedron of O atoms. In reality, there must be water in the structure, and the H atoms cannot be detected with laboratory XRD. Dehydrated MoO_3 should have Mo in octahedral coordination.[45] To make Mo_4O_{11}, a mixture of 15 parts MoO_3 and 1 part Mo metal powder by mass (about 3 atomic % excess Mo compared to a stoichiometric ratio) were ground using an agate mortar and pestle for approximately 20 minutes. The excess Mo was necessary because some of the Mo metal may have been oxidized to begin with, and because stoichiometric drift in the product can be caused by a reaction with the silica tube at high temperatures.[46] Approximately 250 mg of the mixture was pressed into a 6 mm diameter

pellet and sealed under vacuum into a silica ampoule. The ampoule was heated at 800 °C for 2 h in a box furnace and then quenched in room temperature water. A sparkly dark purple product was obtained and stored in a desiccator or Ar-filled glovebox.

Powder X-ray diffraction To confirm the phase purity of the Mo_4O_{11} active material, high-resolution synchrotron powder XRD data were collected at beamline 11-BM at the Advanced Photon Source at Argonne National Laboratory. Rietveld analysis was performed using Topas Academic.[47] Patterns were refined against the previously experimentally determined structure for Mo_4O_{11}.[37] Lattice parameters, atomic positions, and thermal parameters were refined and a pseudo-Voigt peak type was used. The final R_{wp} value (goodness of fit parameter) was 13 %. The refinement parameters are given in Table S1 in the SI, and bond valence summations are given in Table S2.

Microscopy To determine the particle size of the active material, scanning electron microscopy (SEM) was carried out on the cast electrode using a Nova 230 Nano Scanning Electron Microscope at 10 kV. All other images were captured with an FEI Nova Nano 650 FEG SEM at 5 kV acceleration voltage.

Electrochemical characterization The electrochemical performance of Mo_4O_{11} was characterized using coin cells assembled in an Ar-filled glovebox ($H_2O \leq 0.1$ ppm, $O_2 \leq 0.1$ ppm) using polished Li foil as a combined counter and reference electrode. Mo_4O_{11}, carbon black (TIMCAL Super P), and polyvinylidene fluoride (PVDF) were mixed in a mass ratio of 80 % active material, 10 % carbon black, and 10 % polymer binder. 1-Methyl-2-pyrrolidinone (NMP) solvent was added to make a slurry, and mixed for 30 minutes in a Vortex ball milling machine using ZrO_2 balls. The slurry was cast onto Al foil using a doctor blade to make a layer approximately 75 μm thick. The average mass loading for each cell was between 1.5 and 2 mg cm^{-2}. Whatman GF/C glass microfiber filters were used as the separator. The cells were flooded with 1 M $LiPF_6$ in ethylene carbonate and dimethylcar-

bonate (EC/DMC 50/50 *v/v* from Sigma Aldrich) electrolyte. A Neware BTS4000-5V10mA Battery Testing System was used for the galvanostatic cycling, long term cycling, and the rate testing. A BioLogic VMP-300 Potentiostat was used for cyclic voltammetry measurements.

Ex situ samples were made by cycling pellet electrodes in Swagelok-type cells rather than cast electrodes in coin cells to make the material easier to recover after cycling. Mo_4O_{11} was ball milled with carbon black (TIMCAL Super P) for 20 minutes in a 7 cm^3 stainless steel ball mill canister and then ground with polytetraflouroethylene (PTFE with average particle size of 1 μm, Sigma Aldrich) such that the final electrode composition was 80 % active material, 10 % carbon black, and 10 % polymer binder. Thick film electrodes 10 mm in diameter were prepared by pressing pellets from this mixture using a hydrostatic pressure of 1.5 tons. Whatman GF/D glass microfiber filters were used as the separator. The cells were flooded with 1 M $LiPF_6$ in EC/DMC 50/50 *v/v* electrolyte (Sigma Aldrich). Three *ex situ* samples were prepared by cycling at a rate of $C/20$ using a using a BioLogic VSP-1 potentiostat: Mo_4O_{11} discharged to 1.2 V, Mo_4O_{11} recharged to 3.0 V, and Mo_4O_{11} discharged a second time to 1.2 V.

Operando XRD data were collected using a Bruker D8 Advance in Bragg-Brentano geometry using a non-monochromated Cu-Kα source (average wavelength of 1.5418 Å). A custom made, stainless steel, Swagelok-type *operando* cell with a Be window (Materion) approximately 254 μm thick (allows X-ray penetration) was used for galvanostatic cycling. As with the *ex situ* cells, pellet electrodes (80 % active material, 10 % carbon black, and 10 % polymer binder) were used and placed directly onto the Be window. The pellet electrodes were cycled against Li foil using a BioLogic SP-200 potentiostat at a $C/20$ rate with two Whatman glass fiber separators flooded with 1 M $LiPF_6$ in EC/DMC 50/50 *v/v* electrolyte (Sigma Aldrich). A pattern was collected approximately every 20 minutes during the charge and discharge.

Operando synchrotron X-ray powder diffraction data were collected at the Stanford

Synchrotron Radiation Lightsource (SSRL) at the SLAC National Accelerator Laboratory where the *operando* cell could be cycled at higher rates. Cast electrodes were used instead of the pellet electrodes that were used for the *operando* laboratory XRD. Pouch cells were assembled using aluminized bags as the casing, polished lithium foil as the counter electrode, and Mo_4O_{11} as the working electrode (approximately $2\,mg\,cm^{-2}$ loading with 10% carbon black and 10% PVDF by mass supported on Al foil). A Celgard separator soaked in 1 M $LiPF_6$ in EC/DEC (LP40, Gotion) was used between the counter and working electrodes. The cell was assembled and sealed in an Ar-filled glovebox (< 0.1 ppm O_2, < 0.1 ppm H_2O). Once removed from the glovebox, the cell was placed between two stainless steel blocks with Be windows to apply pressure. X-ray powder diffraction was collected at SSRL beamline 11-3 (fixed energy of 12.7 keV) in transmission geometry with a Rayonix MX225 CCD area detector. The cells were cycled at varying rates ($C/5$, $1C$) during data collection using a BioLogic VSP-300 potentiostat. Detector images were collected every 3 minutes, with 10 second exposures. The spot size was 150 μm by 150 μm, and the beam was jogged horizontally by 4 mm during acquisition to achieve a better powder average. The 2D data were reduced to 1D diffraction patterns (intensity versus Q) using pyFAI.[48] Area detector calibration was performed using LaB_6.

As described in the introduction, the theoretical capacity of Mo_4O_{11} is achieved with the transfer of six electrons per formula unit, corresponding to the reduction of all Mo atoms to their 4+ oxidation state. However, following the emerging convention for materials that undergo multielectron redox, C-rates were calculated based on the reduction of one electron per redox-active transition metal. In this case, four Li were assumed to insert into the crystal structure per formula unit for calculating C-rates, for example: $C/5 = 4Q/5 = 192\,mAh\,g^{-1}/(5\text{ h}) = 38.4\,mA\,g^{-1}$, where Q is the charge.

X-ray photoelectron spectroscopy (XPS) XPS was used to investigate how the oxidation state on the Mo redox center changes as the Mo_4O_{11} is discharged and charged. Exposure

to air can also affect the oxidation state on the Mo, so the *ex situ* samples were loaded onto an air-free sample holder in an Ar-filled glovebox ($H_2O \leq 0.1$ ppm, $O_2 \leq 0.1$ ppm). The powder was spread onto double-sided scotch tape attached to a stainless steel sample holder. A lid with an O-ring seal was secured onto the sample holder to transfer the samples into the XPS chamber. Once under vacuum, the lid was removed such that the samples were never exposed to air. The samples were measured using a Thermo Fisher Escalab Xi+ XPS equipped with a monochromated Al anode (E = 1486.7 eV). Survey scans were collected at 100 eV pass energy with 50 ms of dwell time; two scans were averaged. High resolution Mo scans were collected for uncycled Mo_4O_{11}, Mo_4O_{11} discharged to 1.2 V, Mo_4O_{11} recharged to 3.0 V, and Mo_4O_{11} discharged a second time to 1.2 V using a pass energy of 20 eV and a dwell time of 100 ms, averaging 10 scans.

Fits to the data to determine the Mo oxidation state were performed using CasaXPS with Shirley backgrounds and asymmetric Lorentzian line shapes, as has previously been suggested for oxides of Mo.[49] All samples were ball milled with carbon black prior to XPS, so the spectra were referenced to the C 1s peak of graphite and amorphous carbon black at 284.5 eV.[50] The fits of the Mo d-orbital peaks were area-constrained, as the electrons of a d-orbital split into two peaks, Mo $3d_{5/2}$ and Mo $3d_{3/2}$, in a 3:2 area ratio.[51,52] Each pair of peaks was also constrained to have the same full width half max (FWHM). The peak splitting energies determined from the fits were very close to 3.13 eV, especially for Mo^{6+} and Mo^{5+}, which is the average value reported in the NIST X-ray Photoelectron Spectroscopy Database.[53] Peak locations for the Mo^{4+}, Mo^{5+}, and Mo^{6+} peaks were also similar to the locations reported in the literature for Mo oxides.[51,54] Fitting parameters are given in the SI in Table S4.

Raman Spectroscopy Raman spectroscopy measurements were performed using a Horiba Jobin Yvon T64000 open-frame confocal microscope with a triple monochromator and LN2 cooled CCD array detector. Samples were prepared in an Ar-filled glovebox

($H_2O \leq 0.1$ ppm, $O_2 \leq 0.1$ ppm) by sealing a glass coverslip over the powder sample on a glass microscope slide. Data were collected with a 488 nm laser, 1800 cm^{-1} grating and 500 μm slit. The laser intensity was 4 mW for a 2 sec exposure time, and ten spectra were averaged. A short exposure (2 sec) followed by a long exposure (5 sec) spectrum was compared for each sample to verify that the sample did not decompose due to beam exposure.

Transmission Electron Microscopy TEM was conducted using a Thermofisher Talos F200X S/TEM at 200 kV. Two samples were examined with TEM: Mo_4O_{11} after ball milling with carbon black and a Mo_4O_{11} sample that was made into an electrode and discharged to 1.2 V (lithiated) and charged to 3.0 V (delithiated). The powders were gently poured onto a Cu TEM grid inside an Ar glovebox and sealed inside an aluminum laminated pouch. Gentle argon gas flow was maintained around the sample holder to minimize air exposure during sample loading into the microscope.

Potentiometric entropy measurements As another probe into the structural changes occurring during cycling, the open-circuit voltage $U_{OCV}(x,T)$ and the entropic potential $\partial U_{OCV}(x,T)/\partial T$ of a coin cell were measured as functions of Li composition using a potentiometric entropy measurement technique described in previous work.[55,56] The coin cell consisted of a Mo_4O_{11}-based electrode with the same composition as those used for the electrochemical characterization. Li metal was used as the counter electrode and 1 M $LiPF_6$ in EC/DMC 50/50 *v/v* was used as the electrolyte. The potentiometric entropy measurements consisted of imposing a series of constant current pulses lasting 30 minutes, each followed by a relaxation period lasting 270 minutes. For clear characterization of the first lithiation, the first 14 current pulses were imposed at a rate of $C/50$, while the next 80 current pulses were imposed at a rate of $C/25$. During all subsequent cycling, $C/10$ current pulses were applied. During the relaxation periods, a step-like temperature profile was applied to the coin cell from 15 °C to 25 °C in 5 °C increments with a thermoelectric

cold plate (TE technology, CP-121). The corresponding coin cell voltage evolution was recorded with a potentiostat (BioLogic, VSP-300). Before recording the open-circuit voltage $U_{OCV}(x,T)$ and applying the next temperature step, we verified that the coin cell had reached thermodynamic equilibrium by ensuring that (i) the temperature difference between the cold plate and the top of the coin cell was less than 0.1 °C and (ii) the time rate of change of the open-circuit voltage $\partial U_{OCV}(x,T)/\partial t$ was less than 1 mV h^{-1}.

Results and Discussion

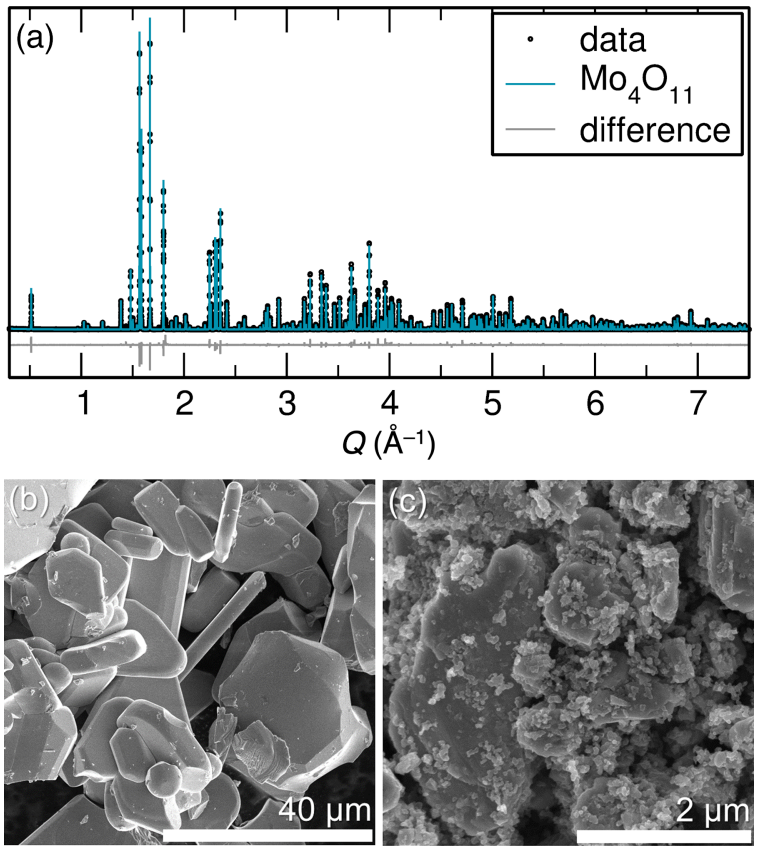

Figure 2: (a) Rietveld refinement of high-resolution synchrotron powder XRD from beamline 11-BM at the Advanced Photon Source revealed the sample to be single phase Mo_4O_{11}. (b) SEM image of the solid-state prepared Mo_4O_{11} particles which range in diameter from 5 to 40 μm. (c) SEM image of the Mo_4O_{11} particles, on the order of 1 μm in size, after being ball milled with carbon black. The Mo_4O_{11} particles that were ball milled in the slurry turned out similar in size, if not slightly larger, ranging in size from 1 to 5 μm – see SI Figure S2.

The phase purity of the prepared Mo_4O_{11}, with the structure described previously, was verified using high-resolution synchrotron powder XRD data from beamline 11-BM at the Advanced Photon Source. The Rietveld refinement is shown in Figure 2(a) and the associated fit parameters are presented in the SI in Table S1. A bond valence analysis of the valence states on Mo in Mo_4O_{11} suggests that three of the four crystallographically distinct Mo sites have valences intermediate between 5+ and 6+. Only one of the three octahedral sites, Mo3 as defined in the SI, has a bond valence sum very close to 6+, and as one would expect, is also the most distorted due to the d^0 electronic configuration. The SEM images of the as-prepared material [Figure 2(b)], the particles after ball milling with carbon black [Figure 2(c)], and the slurry-cast Mo_4O_{11} (SI Figure S2) show that all the electrochemistry was carried out using micron-sized particles.

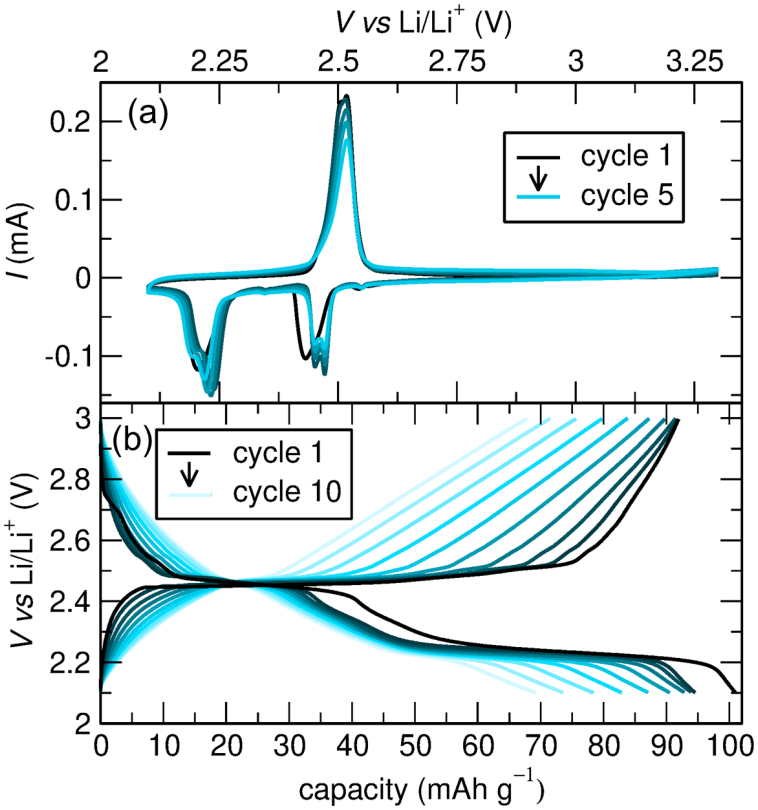

Figure 3: (a) Cyclic voltammetry (CV) of Mo_4O_{11} performed at a scan rate of 0.1 mV s^{-1} from 2.1 V to 3.3 V. (b) Galvanostatic cycling at a rate of $C/10$ first discharging to 2.1 V and then charging to 3.0 V for 10 cycles.

We began electrochemistry experiments, including cyclic voltammetry (CV) in Figure 3(a) and galvanostatic cycling in Figure 3(b), with a lower voltage cutoff of 2.1 V based on literature that reported irreversibility and amorphization of the active material when it was discharged below 2.0 V–2.1 V.[33,44] In this voltage range, the Mo_4O_{11} was not reduced enough to achieve the theoretical capacity, and instead the maximum capacity demonstrated is small, around 100 mAh g^{-1}. Furthermore, based on the even pattern of capacity fade shown in the galvanostatic cycling [Figure 3(b)], it is likely that not all the Li inserted on each discharge is being fully removed in the subsequent charge. The CV appears to suggest a single oxidation peak that could potentially resolve into more peaks for slower sweep rates, or at reduced temperatures. In contrast, there are two clear reduction peaks, pointing to irreversibility in this voltage window that would explain the capacity loss upon repeated cycling. An analysis of variable rate CV by relating the peak current with the scan rate as described previously[10,30,31] (data presented in the SI in Table S3) suggests some ambiguity in determining whether the Li insertion is surface diffusion limited or bulk diffusion limited.

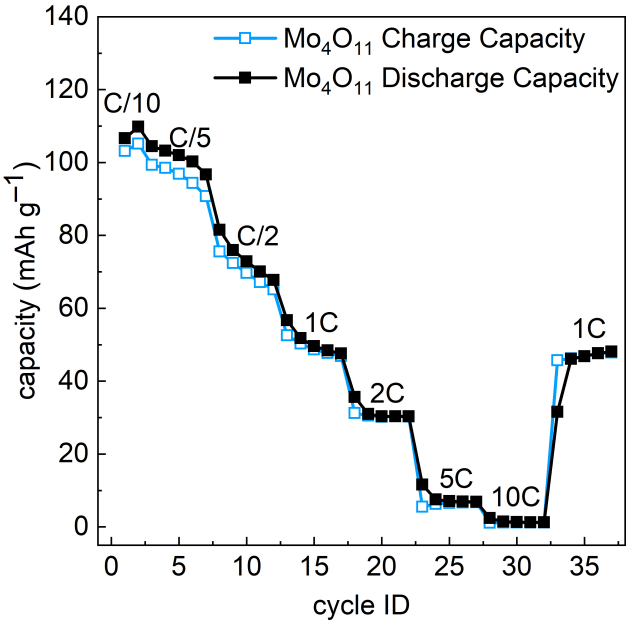

Figure 4: Variable rate galvanostatic cycling of Mo_4O_{11} cycled between 2.1 V and 3.0 V.

The variable rate galvanostatic cycling in the voltage range of 2.1 V to 3 V shown in

Figure 4 demonstrates that the already-low capacity decreases by 50% when the rate is decreased from $C/10$ to $1C$, and then further to nearly zero when the rate is increased to $10C$.

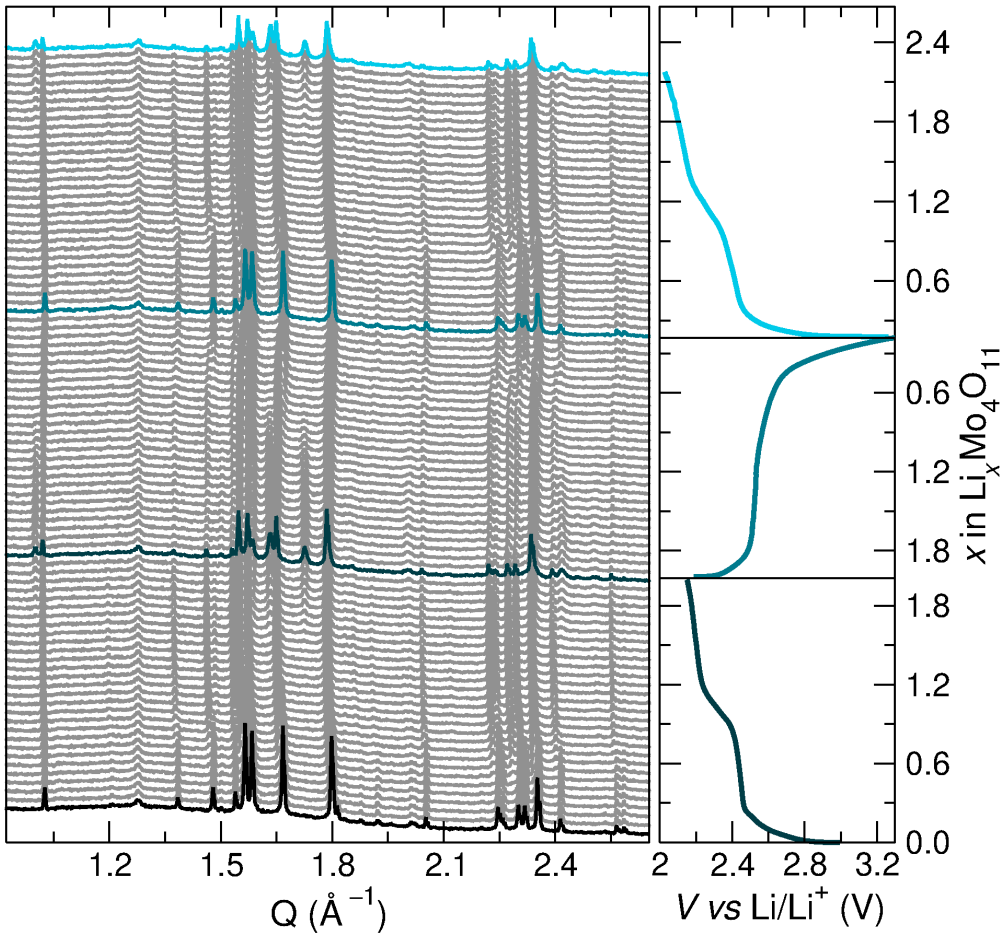

Figure 5: *Operando* XRD of Mo_4O_{11} while the material was discharged to 2.1 V, charged to 3.3 V, and then discharged again at a $C/20$ rate. The peak at $Q = 1.275\,\text{Å}^{-1}$ is an inactive peak associated with the operando cell.

Consistent with a previous structural investigation,[33] however, it is notable that when the discharge is cut off at 2.1 V (at the end of the second voltage plateau), the structural change is completely reversible, as shown by the *operando* XRD in Figure 5. The structural changes above 2.1 V are primarily the same structural peaks as unlithiated Mo_4O_{11}, but shifted to lower angles as the interplanar spacing increases to accommodate the inserted Li. In addition some weaker new reflections that are consistent with the appearance of

two-phase plateaus in the charge/discharge traces appear reversibly around Q = 1.00, 1.75, and 2.45 Å^{-1}.

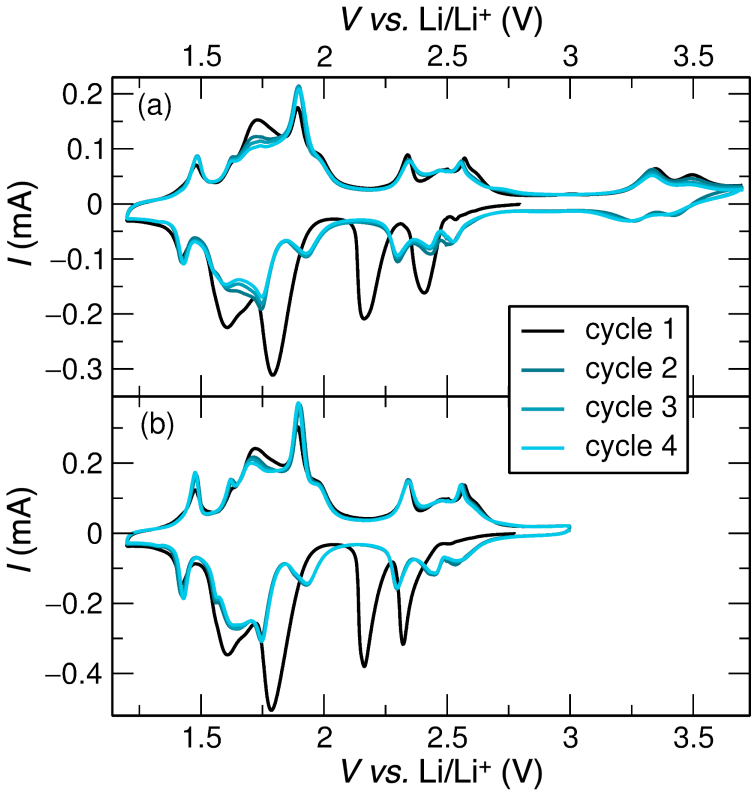

Figure 6: (a) Cyclic voltammetry (CV) of Mo_4O_{11} performed at a scan rate of 0.1 mV s^{-1} from 1.2 V to 3.7 V. (b) CV of Mo_4O_{11} performed at a scan rate of 0.1 mV s^{-1} in a narrower voltage window from 1.2 V to 3.0 V.

A wider voltage window proved necessary to access meaningful capacity in Mo_4O_{11}. CV curves of Mo_4O_{11} discharged down to 1.2 V (Figure 6) are unusually complicated, and revealed many reversible oxidation and reduction peaks after the first cycle. In comparison, MoO_2 only shows two reduction and two oxidation peaks[18] and MoO_3 has only one of each.[26] The complicated CV curves of Mo_4O_{11} indicate that its structure has a more complex variety of Li sites[57] and/or oxidation states on Mo than either MoO_2 or MoO_3 do. As expected, Mo_4O_{11} redox peaks occurred at higher voltages than MoO_2 and at lower voltages than MoO_3 due to the intermediate average oxidation state on Mo. Interestingly, unlike the CV data acquired within the narrower voltage range, presented in Figure 3(a), this CV trace displays some opening around the central region that is characteristic of

pseudocapacitive processes. Figure 6 also compares two different cycling voltage ranges.

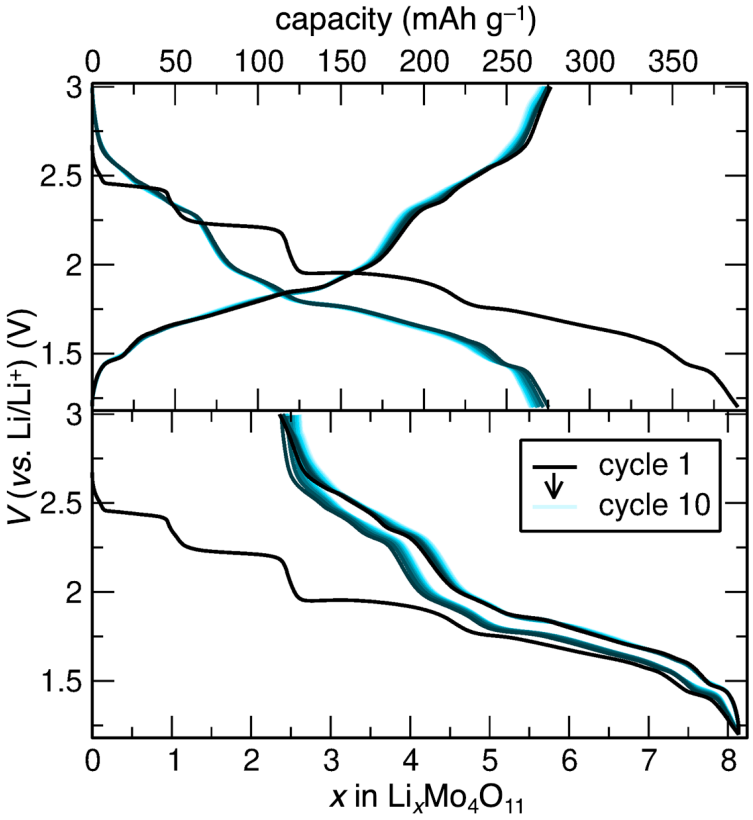

Figure 7: Galvanostatic cycling at a rate of $C/10$ first discharging to 1.2 V and then charging to 3.0 V for 10 cycles.

The 1.2 V to 3 V voltage window was used in all subsequent electrochemistry experiments, including galvanostatic cycling (Figure 7). In this voltage range, the first galvanostatic discharge at $C/10$ achieved a capacity of about 385 mAh g^{-1}, which significantly exceeded the theoretical capacity of 288 mAh g^{-1} but aligned well with first-discharge capacities reported in literature.[33,44] Furthermore, the shape of the first discharge curve looked similar to the literature with respect to number and location of voltage plateaus.[33,34,44] We observed a notable drop in capacity between the first and second discharges which was consistent with the literature.[34,44] However, our cycling stabilized right away to about 270 mAh g^{-1} and then faded very slowly when cycled at a $C/10$ rate, whereas in previous cycling shown in the literature, the capacity faded much more quickly and consistently.[44] This is likely due to our more favorable choice of voltage window. A conversion reaction

was expected at low voltages, so we did not cycle below 1.2 V, while some of the only reported long term cycling dipped down to 0.5 V.[44] The study that cycled between 1.5 V and 3.0 V demonstrated less severe capacity fade,[34] but still more than we observed. This could still be due to the non-optimized voltage window, and our more modern cell configuration. We compared two different upper voltage cutoffs, 3.0 V and 3.7 V, from which we selected 3.0 V for future experiments because it yielded more stable cycling in the long term (see Figure 8(a) compared with 1.2 V to 3.7 V long-term cycling shown in the SI, Figure S3). This could mean that a detrimental or irreversible reaction occurred between 3.0 V and 3.7 V, causing the cell using the wider voltage to experience faster capacity fade. The small oxidation and reduction peaks in the CV between 3.0 V and 3.7 V could be related to dissolution of the active material, which would result in the observed capacity fade, and has also been hypothesized as a failure mode of related MoO_2 batteries.[21] Furthermore, when deconstructing Swagelok cells of Mo_4O_{11} that had been charged up to 3.7 V, the white glass fiber separators were observed to have been stained bright blue, which can indicate dissolution of the active material. This was seemingly avoided when 3.0 V was used as the upper voltage cutoff.

In the CV and galvanostatic cycling experiments, relatively low voltage polarization was observed, which is usually interpreted as a sign of high conductivity of both Li^+–ions and electrons in the material. High conductivity is necessary to achieve the good rate performance exhibited in Figure 8(b). The capacity of the $C/10$ cycling in the rate experiment differs somewhat from the capacity measured during the longer term $C/10$ cycling given in Figure 7, and this difference can be attributed to variation in the mass loading of electrodes cast in different batches. Compared to the second cycle capacity at $C/10$, approximately 88% of the capacity was retained when cycling 10 times faster at a $1C$ rate. At the high rate of $10C$, Mo_4O_{11} still achieved a capacity of 177 mAh g^{-1}. The capacity at a rate of $1C$ was almost entirely recovered after faster cycling (decreased from about 267 mAh g^{-1} to 263 mAh g^{-1}), indicating that the material was not degrading at

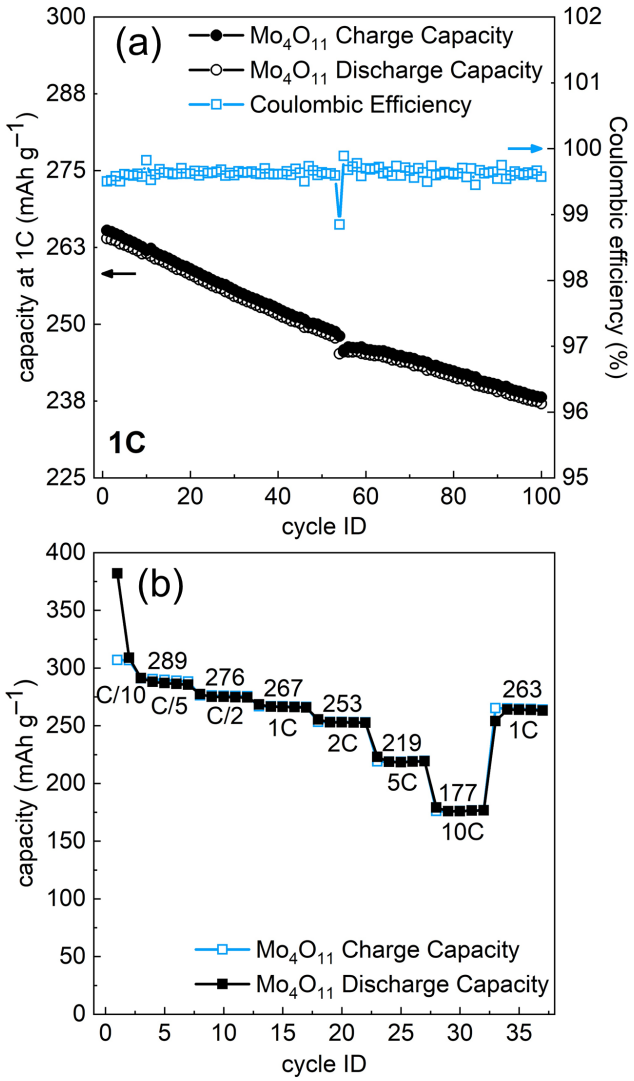

Figure 8: (a) Long-term galvanostatic cycling of Mo_4O_{11} at $1C$ between 1.2 V and 3.0 V. (b) Variable rate galvanostatic cycling of Mo_4O_{11} cycled between 1.2 V and 3.0 V.

higher cycling rates.

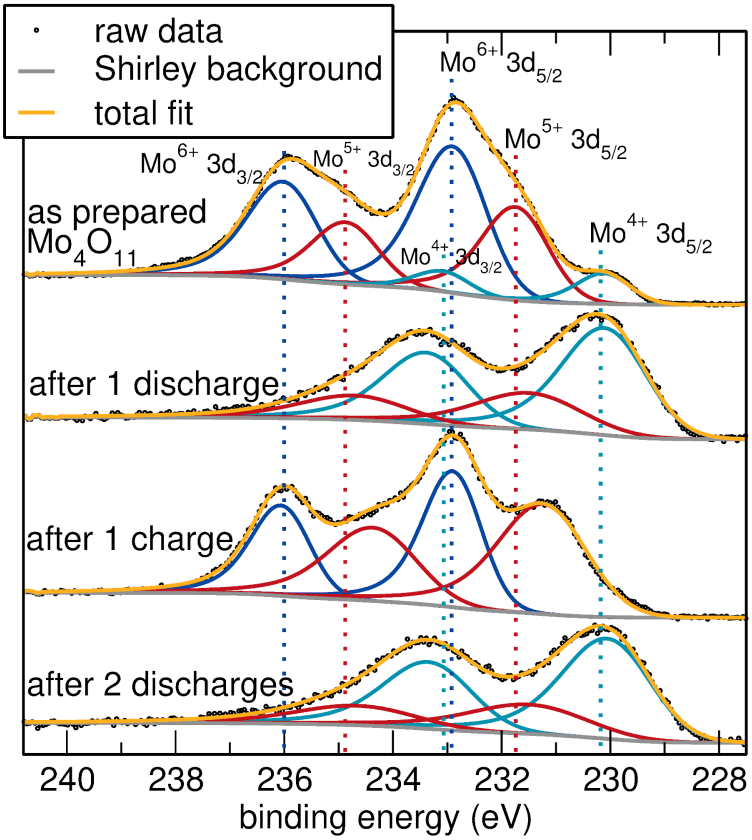

Figure 9: X-ray photoelectron spectra of uncycled Mo_4O_{11}, Mo_4O_{11} discharged to 1.2 V, Mo_4O_{11} recharged to 3.0 V, and Mo_4O_{11} discharged a second time to 1.2 V.

Though the first discharge exceeds the theoretical capacity (which was calculated such that each Mo is in a 4+ oxidation state but none are reduced further), *ex situ* XPS (Figure 9) confirms that the oxidation state of Mo does not go below Mo^{4+}. This means that there must be some other reaction at the Mo_4O_{11} electrode using electrons. Oxygen evolution is unlikely at such low voltages, so it is possible that some solid electrolyte interface layer is forming.

When the cell is recharged, the Mo return to predominantly Mo^{6+} and Mo^{5+}. The XPS spectra of material discharged once versus discharged twice look identical, indicating reversibility after the first discharge.

Structural characterization is key to our task of learning which structural motifs lead to the favorable electrochemical properties we observe. *Operando* XRD is a unique technique

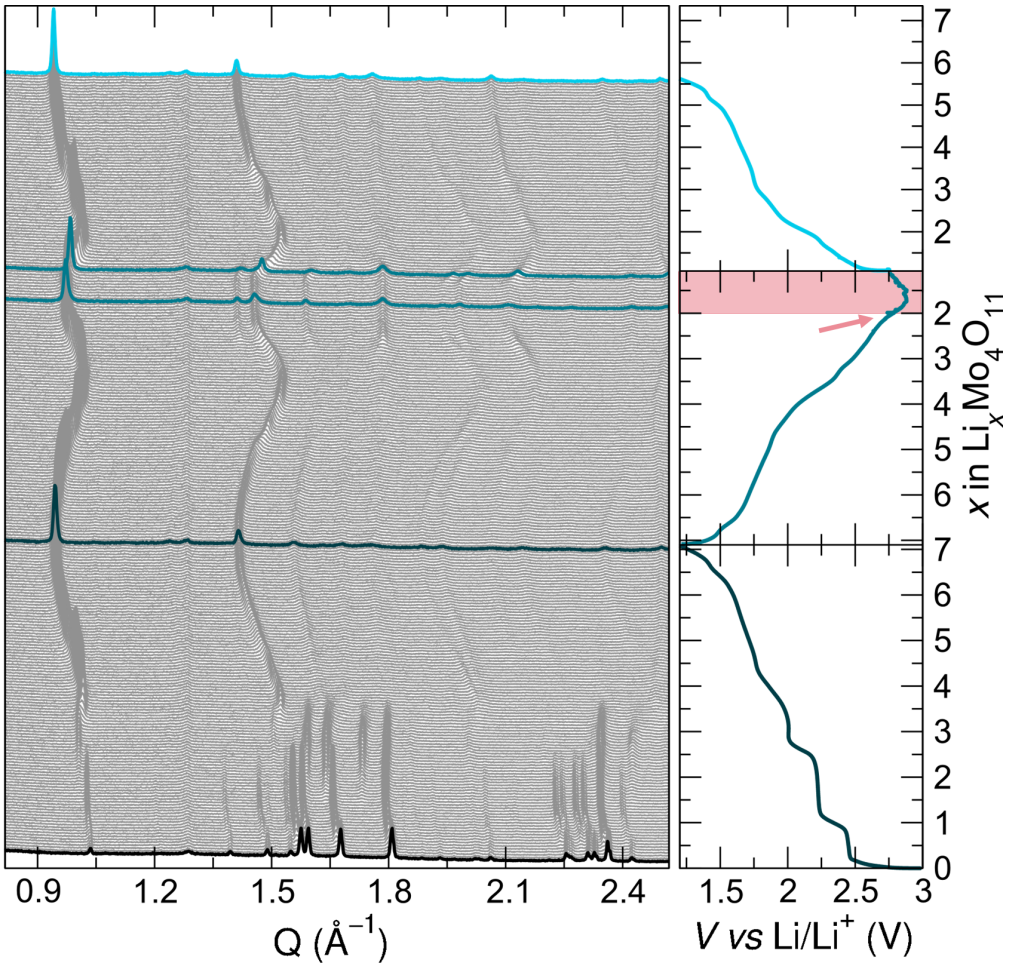

Figure 10: *Operando* XRD of Mo_4O_{11} discharged to 1.2 V, charged to 3.0 V, and discharged again at a $C/20$ rate. The cell underwent a short-circuit at the end of the charge, as marked with the arrow and the shaded box. The structure before and after the short is essentially the same, and the first charge and second discharge show near-identical, repeatable structural evolution. The peak at $Q = 1.275\,\text{Å}^{-1}$ is an inactive peak associated with the *operando* cell.

that allows structural characterization of the electrode material while lithium is being intercalated and deintercalated. Previous *in situ* XRD of orthorhombic Mo_4O_{11} concluded that the structure becomes amorphous during the first discharge below 2 V.[44] In contrast, we observe a complete structural change during the first discharge (Figure 10) but *not* a loss of crystallinity. The structure of this new phase that is formed upon lithiation is then maintained reversibly in subsequent cycling. *Operando* synchrotron XRD was measured for two full cycles at a rate of $C/5$ and for 5+ cycles at $1C$, and at these faster rates the progression of peaks was just as reversible (see SI, Figure S4). Because the new phase is present for all of the cycling except for the first discharge, it is this new phase which demonstrates high capacity at the high rates shown in Figure 8(b). However, the precise structure of this new phase has not yet been determined. While the presence of a strong low angle peak (at around $Q = 1\,\text{Å}^{-1}$, shifted higher or lower depending on how lithiated the structure is) is similar to the layered phases of lithiated MoO_3[29] and $LiMoO_2$,[58] that is where the similarities end. The new phase appearing on discharge of Mo_4O_{11} does not seem to match any lithated or unlithiated Mo oxide phase reported in the Inorganic Crystal Structure Database. While $(Na/Li)_{0.9}Mo_6O_{17}$ have purple bronze structures similar to the unlithiated, monoclinic phase of Mo_4O_{11},[59–62] they do not appear similar to the cycled orthorhombic Mo_4O_{11} structure. We have also compared simulated diffraction patterns from some of the Mo oxide-hydroxide phases to our data, but with no success. The *operando* XRD pattern taken from the delithiated Mo_4O_{11} at the end of the first full cycle but before the cell short-circuit was indexed, and a space group and unit cell are proposed for the new structure later on in this text.

In addition to the phase change, the bow-shaped evolution of peaks during the first charge and second discharge is very unusual. The behavior indicates that the size of the unit cell of the structure is not proportional to the amount of Li in the structure. The *operando* XRD of Mo_4O_{11} shows that once Li starts to be removed from the fully discharged structure, the structure contracts, as expected. However, as delithiation continues past

approximately 2.3 V, the peaks start shifting to a lower angle again, indicating that the structure is expanding as more Li is removed. Interestingly, the lattice spacing of the lithiated and delithiated structures is not very different, when usually a lithiated structure is approximately 10% larger than its delithiated counterpart.

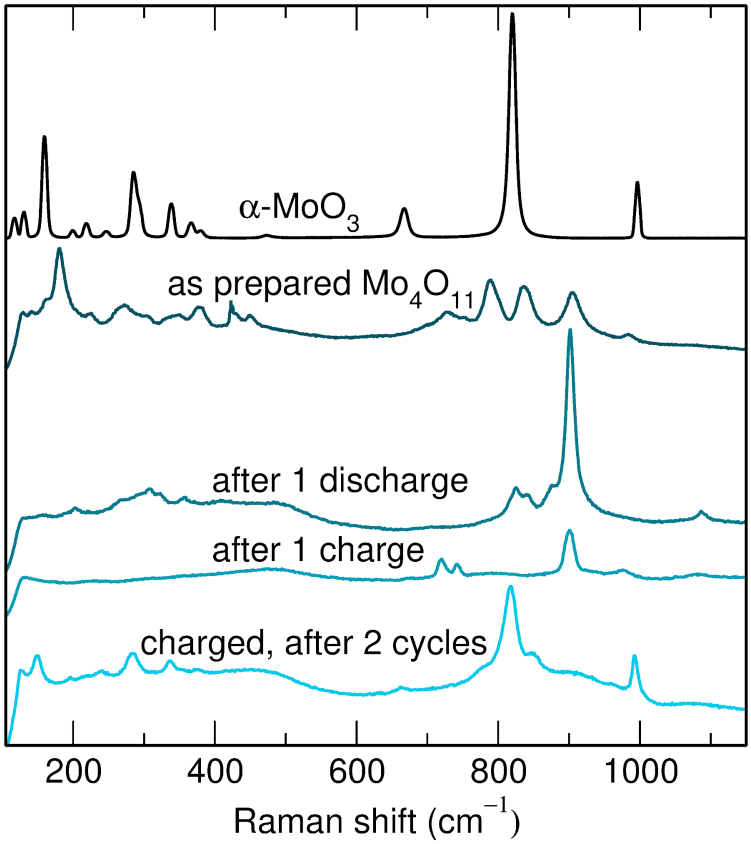

Figure 11: Raman spectra of MoO_3 and uncycled Mo_4O_{11} compared with *ex situ* samples of Mo_4O_{11} cycled between 1.2 V and 3 V at a rate of $C/20$.

In order to further probe the structural transformation of the first discharge past 2 V, *ex situ* Raman spectroscopy was performed on a fully discharged sample, a charged sample, and a sample that had been through two full lithiation and delithiations and compared to spectra from uncycled Mo_4O_{11} and MoO_3 (see Figure 11). We utilized Raman spectroscopy because it can reveal elements of the local structure that may not be captured by XRD which looks at extended crystal symmetry. It is notable that there are clear differences between all three *ex situ* Raman spectra, given that *operando* XRD and entropic potential

measurements show the most drastic structural changes occurring during the first discharge. This suggests that the local structure may continue to change during subsequent cycling without drastically affecting long range order.

The Raman spectrum of as-prepared Mo_4O_{11} has three main peaks at 788, 836, and 906 cm^{-1} originating from doubly coordinated oxygen Mo-O-Mo bonds at corner-shared octahedral sites.[63] The strong peak at 183 cm^{-1} is a characteristic vibration of tetrahedral Mo^{+4}. The dehydrated α-MoO_3 structure is layered and made up of only octahedral Mo sites, and its Raman spectrum is well studied;[64,65] where the 996 cm^{-1} peak is assigned to the stretching modes of Mo=O, the intense peak at 820 cm^{-1} is assigned to the bridging oxygen vibrations (Mo-O-Mo), the 667 cm^{-1} peak to O–Mo–O stretch, and 159 cm^{-1} is a translational rigid MoO_4 chain mode. The twice-cycled Mo_4O_{11} *ex situ* sample has three similar peaks to the α-MoO_3 at 992, 818, 337, and 283 cm^{-1}. The disappearance of the 183 cm^{-1} peak (tetrahedral Mo^{+4}) compared to the uncycled material and the appearance of the 992 cm^{-1} peak (Mo=O) could be further evidence that the transformed Mo_4O_{11} structure is more layered than the pristine orthorhombic Mo_4O_{11}, and/or has a greater fraction of octahedral versus tetrahedral sites than the uncycled Mo_4O_{11}. This concept is not new for Mo, as there is other literature evidence that Mo can change its local environment quite drastically during electrochemical cycling.[66] In the case of $Al_2(MoO_4)_3$, Mo ions also migrated out of tetrahedral sites and into octahedral positions during cycling.[66] However, $Al_2(MoO_4)_3$ became amorphous upon lithiation,[66] while Mo_4O_{11} maintained crystallinity and demonstrated more stable long term cycling. While Raman spectroscopy cannot tell us exactly what the new Mo_4O_{11} structure is, information about the local environment supports that the structure became more layered after the first discharge.

In an attempt to further understand the nature of the structural transformation, transmission electron microscopy was carried out on samples before and after Li^+-cycling. TEM images are shown comparing pristine Mo_4O_{11} after ball milling with carbon black [Figure 12(a)] with an an *ex situ* sample that was lithiated (discharged to 1.2 V) and delithi-

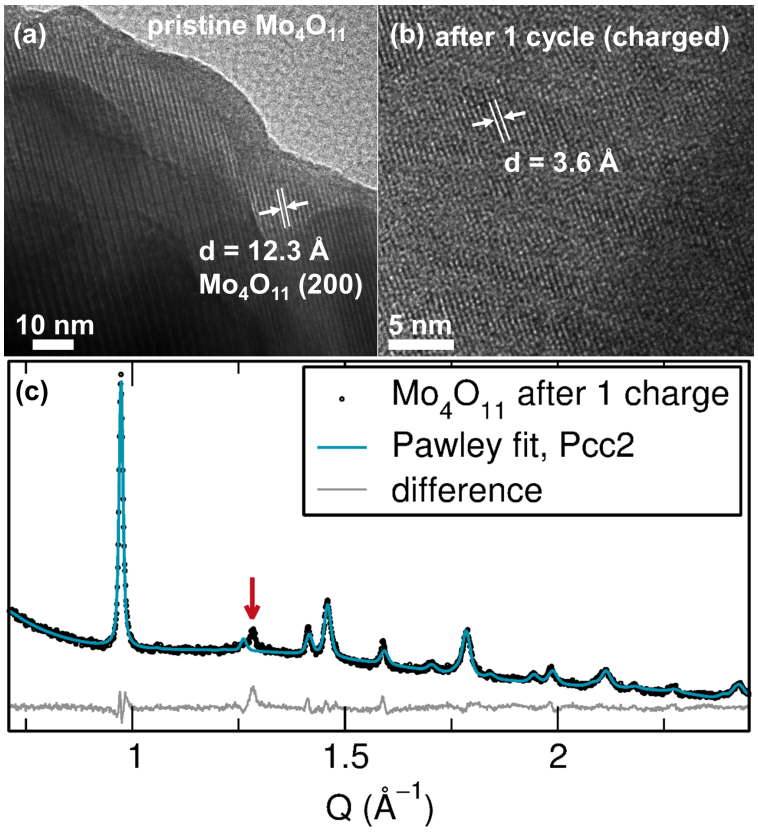

Figure 12: (a) TEM of pristine Mo_4O_{11} after ball milling with carbon black. (b) TEM of an *ex situ* sample of Mo_4O_{11} that was discharged to 1.2 V and then charged to 3 V (delithiated) at a rate of $C/20$. (c) Pawley fit of an XRD pattern taken from the *operando* experiment in Figure 10 at the end of the first charge (before the short-circuit of the cell) in the space group $Pcc2$ and a unit cell with the parameters $a = 25.8787$ Å, $b = 6.1166$ Å, $c = 4.6820$ Å. The arrow points to an inactive peak associated with the *operando* cell.

ated again (charged to 3.0 V) [Figure 12(b)]. Figure 12(a) confirms the d-spacing of 12.3 Å expected between the pristine Mo_4O_{11} 200 planes. The d-spacing of 3.6 Å measured in Figure 12(b) matches the d-spacing expected from the peak at $Q = 1.787\,\text{Å}^{-1}$ in the *operando* XRD pattern taken at the same state of charge (delithiated Mo_4O_{11} at the end of the first full cycle). The same *operando* XRD pattern was indexed in Topas Academic,[47] and the space groups and unit cells that seemed to most logically fit the data were: $Pcc2$ with $a = 25.8787$ Å, $b = 6.1166$ Å, $c = 4.6820$ Å, cell volume = 741.102 Å^3 and and $Pmc21$ with $a = 25.9476$ Å, $b = 6.1281$ Å, $c = 4.1803$ Å, cell volume = 664.710 Å^3. Figure 12(c) shows a Pawley fit of the data using the $Pcc2$ space group, and all the sample peaks are fit by the model. This greatly narrows down the options for the possible structure of the cycling Mo oxide phase. However, with the existing data, the complete structure, given the indication of a large unit cell, appears out of reach at this time.

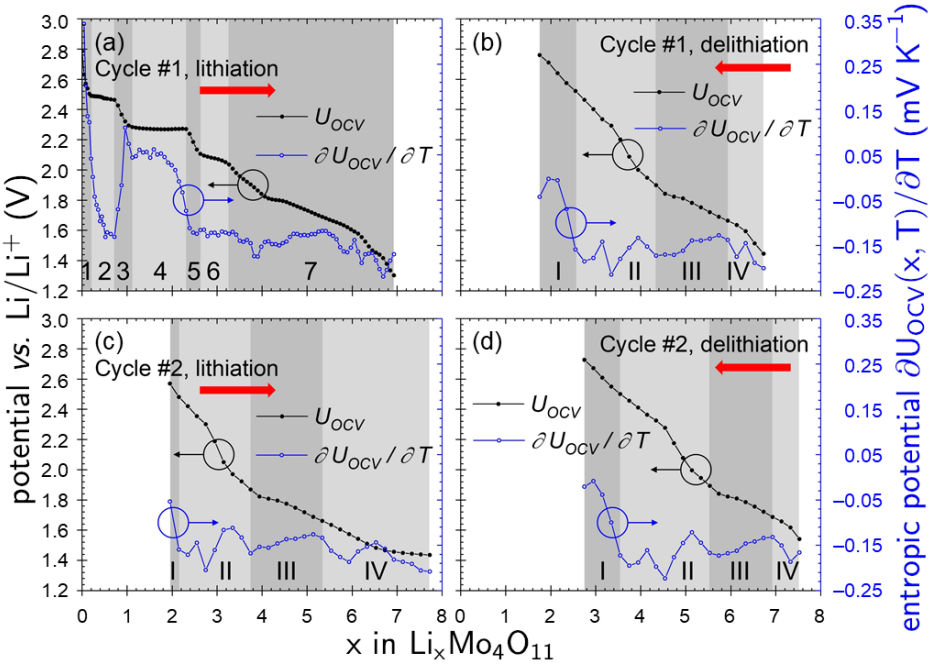

Figure 13: Open-circuit voltage $U_{OCV}(x,T)$ and entropic potential $\partial U_{OCV}(x,T)/\partial T$ of Mo_4O_{11} coin cell as functions of lithium composition x in $Li_xMo_4O_{11}$. The different processes involved in panels (a) through (d) are indicated in the figure. Note the regions labeled 1 through 7 in panel (a) are distinct from the regions labeled I through IV in panels (b), (c), and (d).

Entropic potential measurements confirmed that the structure changes completely on first lithiation below 2.0 V to a structure that then cycles reversibly. Figure 13 plots the open-circuit voltage $U_{OCV}(x,T)$ and the entropic potential $\partial U_{OCV}(x,T)/\partial T$ of the Mo_4O_{11} coin cell as a function of lithium composition x in $Li_xMo_4O_{11}$ for the first two full cycles. Figure 13(a) shows that during the first discharge/lithiation, seven distinct regions could be identified based on the evolution of $U_{OCV}(x,T)$ and $\partial U_{OCV}(x,T)/\partial T$. In region 1 ($0 < x < 0.2$), both $U_{OCV}(x,T)$ and $\partial U_{OCV}(x,T)/\partial T$ dropped sharply, indicating lithium insertion in a homogeneous solid solution.[55,56] In region 2 ($0.2 < x < 0.7$), both $U_{OCV}(x,T)$ and $\partial U_{OCV}(x,T)/\partial T$ featured a plateau, corresponding to a two-phase coexistence region.[55,56] In region 3 ($0.7 < x < 1.1$), the decreasing $U_{OCV}(x,T)$ suggests a homogeneous solid solution. Meanwhile, $\partial U_{OCV}(x,T)/\partial T$ first increased then decreased resulting in a local maximum. This behavior might be due to an increase in the electrical conductivity, which would lead to an increase in the electronic entropy.[55,56] Both region 4 ($1.1 < x < 2.3$) and region 6 ($2.6 < x < 3.3$) featured two-phase coexistence similar to region 2, while region 5 ($2.3 < x < 2.6$) featured a homogeneous solid solution similar to region 1. Finally in region 7 ($3.3 < x < 6.9$), the sloped $U_{OCV}(x,T)$ suggests a homogeneous solid solution. Furthermore, $\partial U_{OCV}(x,T)/\partial T$ exhibited tilde-shaped fluctuations, which can be attributed to intralayer lithium ordering.[55,56,67,68] Experimentally, redox peaks are observed in cyclic voltammetry at the potential where ion ordering occurs. This result indicates that the ion ordering reaction can possibly enhance the specific capacity. Similarly, Figure 13 shows (b) the first delithiation/charge, (c) the second lithiation/discharge, and (d) the second delithiation/charge. In Figure 13 (b)-(d), only four distinct regions could be identified. To highlight the change in behavior after the first lithiation, the different regions were numbered using Roman numerals instead of numbers 1-7 for the first lithiation. All four regions featured homogeneous solid solution behavior, but regions II and IV also featured intralayer lithium ordering based on the tilde-shaped fluctuations in $\partial U_{OCV}(x,T)/\partial T$.[56,69] In general terms, the voltage regions showing homogeneous solid solutions and two-phase

coexistence during the first two cycles are in agreement with electrochemical testing. In the CV we can see redox peaks around the same potentials as both the two-phase coexistence regions and the ion ordering regions. Consistent with the *operando* XRD, the evolution of $U_{OCV}(x,T)$ and $\partial U_{OCV}(x,T)/\partial T$ significantly changed during the first lithiation, but then remained similar during the subsequent cycling, indicating reversibility after the first discharge.

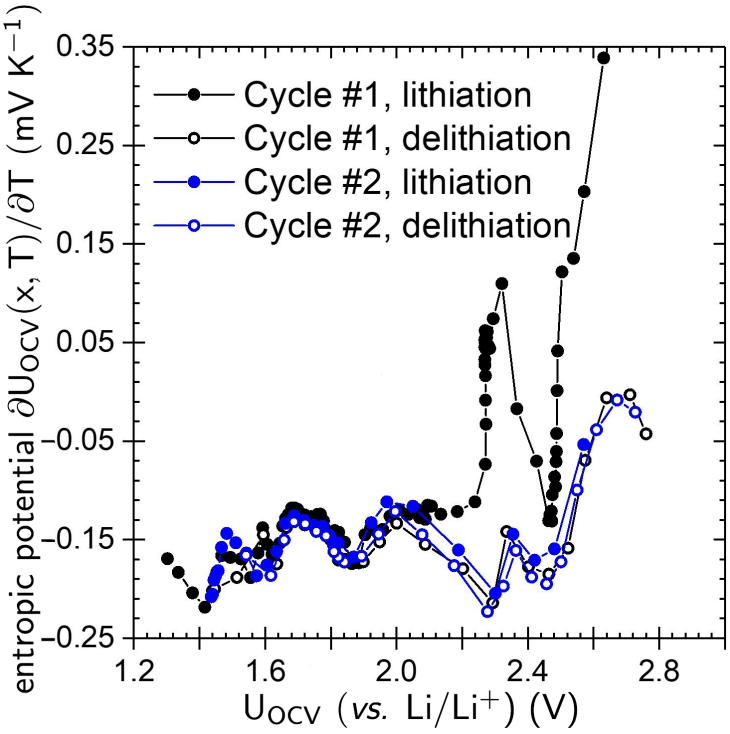

Figure 14: Entropic potential $\partial U_{OCV}(x,T)/\partial T$ of a Mo_4O_{11} coin cell as a function of open-circuit voltage $U_{OCV}(x,T)$ during the first two cycles.

For further illustration, Figure 14 overlays the entropic potential $\partial U_{OCV}(x,T)/\partial T$ of the Mo_4O_{11} coin cell as a function of the open-circuit voltage $U_{OCV}(x,T)$ for the first two cycles. All the traces, except for the first lithiation above 2.1 V are overlapping. This is further support that entropy profile plots of $\partial U_{OCV}(x,T)/\partial T$ vs. $U_{OCV}(x,T)$ can reveal fundamental changes in the structure and the thermodynamics of the material beyond the degradation caused by increasing kinetic barriers.[70] Overall, the potentiometric entropy measurements confirm the existence of homogeneous solid solution and two-phase coex-

istence which were also identified from electrochemical testing, and capture the existence of intralayer ion ordering which was not identifiable from other characterization methods. They also support the finding that Mo_4O_{11} undergoes an irreversible phase change during the two-phase coexistence region of the first lithiation, but the structure and the thermodynamics of the new phase remain stable during the subsequent cycling.

Conclusions

In this study, the reduced molybdenum oxide Mo_4O_{11} has been prepared and characterized as a high-rate Li^+–ion battery electrode. Redox occurs on the Mo centers, going from Mo^{6+} to Mo^{4+}. With higher oxidation states than Nb, this puts the redox occurring in Mo_4O_{11} at a higher voltage than many of the high rate shear-structured materials, making it less effective as an anode. However, this material teaches us many structural lessons. Despite the lack of apparent electronic conduction pathways through the orthorhombic Mo_4O_{11} structure (no edge sharing), a capacity of over 200 mAh g^{-1} was achieved at the high rate of $5C$ using micron-sized particles of the active material. *Operando* XRD and entropic potential measurements reveal that the structure dramatically changes upon the first lithiation, and subsequent cycling is completely reversible with low capacity fade. It is this new structure that demonstrates high-rate cycling and extremely little voltage polarization. This finding greatly expands the scope of candidate high-rate electrode materials to those whose structures may become more favorable with lithium insertion. The new structure of Mo_4O_{11} after the first discharge could not yet be precisely determined from the *operando* XRD experiment; however, the XRD pattern from the delithiated material was indexed and possible space groups of $Pcc2$ and $Pmc2_1$ were proposed. The strong low angle XRD peaks and the similarity of the *ex situ* Raman spectra of the twice cycled Mo_4O_{11} to that of MoO_3 suggest that the structure may become more layered, with a greater fraction of Mo in octahedral rather than tetrahedral sites. A major goal of materials research is to determine

which structural motifs lead to which properties, so determining the precise structure that appears after the first discharge would be a very important continuation to this study. The ability to design high-power battery materials can lead us to next-generation energy storage and electric vehicles.

Supporting Information Available

Powder XRD of the dehydrated MoO_3 precursor. Refinement parameters for the Mo_4O_{11} powder synchrotron X-ray diffraction data. Bond valence sum analysis of orthorhombic Mo_4O_{11}. SEM image of the Mo_4O_{11} that was ball milled in the form of a slurry. Long term cycling of Mo_4O_{11} between 1.2 V and 3.7 V. Table describing the fits to current peaks in the variable rate cyclic voltammetry within the limited voltage range. Cyclic voltammograms between 2.1 V and 3.3 V. XPS fitting parameters.

Acknowledgement

RCV would like to acknowledge Dr. Brenden Ortiz for patient guidance with fitting and indexing peaks from XRD data for crystal structure determination. This work was supported as part of the Center for Synthetic Control Across Length-scales for Advancing Rechargeables (SCALAR), United States, an Energy Frontier Research Center funded by the U.S. Department of Energy, Office of Science, Basic Energy Sciences under DE-SC0019381. The research reported here made use of shared facilities of the UC Santa Barbara National Science Foudation (NSF) – supported Materials Research Science and Engineering Center (DMR 1720256), a member of the Materials Research Facilities Network (www.mrfn.org), as well as use of the Nanostructure Cleanroom Facility within the California NanoSystems Institute, supported by the University of California, Santa Barbara and the University of California, Office of the President. RCV acknowledges the NSF for a graduate research

fellowship (DGE-2139319). JLA acknowledges the NSF for a graduate research fellowship (DGE-1842487). Use of the Advanced Photon Source at Argonne National Laboratory was supported by the U. S. Department of Energy, Office of Science, Office of Basic Energy Sciences, under Contract No. DE-AC02-06CH11357. TEM experiments were conducted at the San Diego Nanotechnology Infrastructure (SDNI) of UCSD, a member of the National Nanotechnology Coordinated Infrastructure, which is supported by the National Science Foundation (Grant No. ECCS-1542148). Use of the Stanford Synchrotron Radiation Lightsource, SLAC National Accelerator Laboratory, is supported by the U.S. Department of Energy, Office of Science, Office of Basic Energy Sciences under Contract No. DE-AC02-76SF00515.

References

(1) Agency, U. S. E. P. Inventory of U.S. Greenhouse Gas Emissions and Sinks: 1990–2019. 2021.

(2) Liu, Y.; Zhu, Y.; Cui, Y. Challenges and Opportunities Towards Fast-charging Battery Materials. *Nat. Energy* **2019**, *4*, 540–550.

(3) Hyde, B. G.; Bagshaw, A. N.; Andersson, S.; O'Keeffe, M. Some Defect Structures in Crystalline Solids. *Annu. Rev. Mater. Sci.* **1974**, *4*, 43–92.

(4) Gopalakrishnan, J. Insertion/Extraction of Lithium and Sodium in Transition Metal Oxides and Chalcogenides. *Bull. Mater. Sci.* **1985**, *7*, 201–214.

(5) Han, J.-T.; Huang, Y.-H.; Goodenough, J. B. New Anode Framework for Rechargeable Lithium Batteries. *Chem. Mater.* **2011**, *23*, 2027–2029.

(6) Han, J.-T.; Goodenough, J. B. 3-V Full Cell Performance of Anode Framework $TiNb_2O_7$/Spinel $LiNi_{0.5}Mn_{1.5}O_4$. *Chem. Mater.* **2011**, *23*, 3404–3407.

(7) Griffith, K. J.; Senyshyn, A.; Grey, C. P. Structural Stability from Crystallographic Shear in TiO_2-Nb_2O_5 Phases: Cation Ordering and Lithiation Behavior of $TiNb_{24}O_{62}$. *Inorg. Chem.* **2017**, *56*, 4002–4010.

(8) Griffith, K. J.; Wiaderek, K. M.; Cibin, G.; Marabella, L. E.; Grey, C. P. Niobium Tungsten Oxides for High-Rate Lithium-Ion Energy Storage. *Nature* **2018**, *559*, 556–563.

(9) Griffith, K. J.; Wiaderek, K. M.; Cibin, G.; Marbella, L. E.; Grey, C. P. Niobium Tungsten Oxides for High-Rate Lithium-Ion Energy Storage. *Nature* **2018**, *559*, 556–563.

(10) Preefer, M. B.; Saber, M.; Wei, Q.; Bashian, N. H.; Bocarsly, J. D.; Zhang, W.; Lee, G.; Milam-Guerrero, J.; Howard, E. S.; Vincent, R. C.; Melot, B. C.; Van der Ven, A.;

Seshadri, R.; Dunn, B. S. Multielectron Redox and Insulator-to-Metal Transition upon Lithium Insertion in the Fast-Charging, Wadsley-Roth Phase PNb_9O_{25}. *Chem. Mater.* **2020**, *32*, 4553–4563.

(11) Griffith, K. J.; Grey, C. P. Superionic Lithium Intercalation through 2×2 nm^2 Columns in the Crystallographic Shear Phase $Nb_{18}W_8O_{69}$. *Chem. Mater.* **2020**, *32*, 3860–3868.

(12) Wyckoff, K. E.; Robertson, D. D.; Preefer, M. B.; Teicher, S. M. L.; Bienz, J.; Kautzsch, L.; Mates, T. E.; Cooley, J. A.; Tolbert, S. H.; Seshadri, R. High-Capacity Li^+ Storage through Multielectron Redox in the Fast-Charging Wadsley-Roth Phase $(W_{0.2}V_{0.8})_3O_7$. *Chem. Mater.* **2020**, *32*, 9415–9424.

(13) McColl, K.; Griffith, K. J.; Dally, R. L.; Li, R.; Douglas, J. E.; Poeppelmeier, K. R.; Cora, F.; Levin, I.; Butala, M. M. Energy Storage Mechanisms in Vacancy-Ordered Wadsley-Roth Layered Niobates. *J. Mater. Chem. A* **2021**, *9*, 20006–20023.

(14) Voskanyan, A. A.; Navrotsky, A. Shear Pleasure: The Structure, Formation, and Thermodynamics of Crystallographic Shear Phases. *Annu. Rev. Mater. Res.* **2021**, *51*, 521–540.

(15) Magnéli, A. The Crystal Structures of Mo_9O_{26} (β'-Molybdenum Oxide) and Mo_8O_{23} (β-Molybdenum Oxide). *Acta Chem. Scand.* **1948**, *2*, 501–517.

(16) Auborn, J. J.; Barberio, Y. L. Lithium Intercalation Cells Without Metallic Lithium. *J. Electrochem. Soc.* **1987**, *134*, 638–641.

(17) Dahn, J. R.; McKinnon, W. R. Structure and Electrochemistry of Li_xMoO_2. *Solid State Ion.* **1987**, *23*, 1–7.

(18) Shi, Y.; Guo, B.; Corr, S. A.; Shi, Q.; Hu, Y.-S.; Heier, K. R.; Chen, L.; Seshadri, R.; Stucky, G. D. Ordered Mesoporous Metallic MoO_2 Materials with Highly Reversible Lithium Storage Capacity. *Nano Lett.* **2009**, *9*, 4215–4220.

(19) Ji, X.; Herle, P. S.; Rho, Y.; Nazar, L. F. Carbon/MoO_2 Composite Based on Porous Semi-Graphitized Nanorod Assemblies from In Situ Reaction of Tri-Block Polymers. *Chem. Mater.* **2007**, *19*, 374–383.

(20) See, K. A.; Lumley, M. A.; Stucky, G. D.; Grey, C. P.; Seshadri, R. Reversible Capacity of Conductive Carbon Additives at Low Potentials: Caveats for Testing Alternative Anode Materials for Li-Ion Batteries. *J. Electrochem. Soc.* **2017**, *164*, A327–A333.

(21) Takeuchi, M.; Fujimoto, H.; Kida, Y. Cycle Performance and Molybdenum Dissolution into Electrolyte in MoO_2 Anode for Lithium Secondary Batteries. *ECS Meet. Abstr.* **2010**, *218*, 1101.

(22) Besenhard, J. O.; Heydecke, J.; Fritz, H. P. Characteristics of Molybdenum Oxide and Chromium Oxide Cathodes in Primary and Secondary Organic Electrolyte Lithium Batteries. I. Morphology, Structure, and Their Changes During Discharge and Cycling. *Solid State Ion.* **1982**, *6*, 215–224.

(23) Saji, V. S.; Lee, C.-W. Molybdenum, Molybdenum Oxides and Their Electrochemistry. *ChemSusChem* **2012**, *5*, 1146–1161.

(24) Campanella, L.; Pistoia, G. MoO_3: A New Electrode Material for Nonaqueous Secondary Battery Applications. *J. Electrochem. Soc.* **1971**, *118*, 1905–1908.

(25) Dampier, F. W. The Cathodic Behavior of CuS, MoO_3, and MnO_2 in Lithium Cells. *J. Electrochem. Soc.* **1974**, *121*, 656–660.

(26) Chen, J. S.; Cheah, Y. L.; Madhavi, S.; Lou, X. W. Fast Synthesis of α-MoO_3 Nanorods with Controlled Aspect Ratios and Their Enhanced Lithium Storage Capabilities. *J. Phys. Chem. C* **2010**, *114*, 8675–8678.

(27) Mai, L.; Hu, B.; Chen, W.; Qi, Y.; Lao, C.; Yang, R.; Dai, Y.; Wang, Z. L. Lithi-

ated MoO_3 Nanobelts with Greatly Improved Performance for Lithium Batteries. *Adv. Mater.* **2007**, *19*, 3712–3716.

(28) Zhou, L.; Yang, L.; Yuan, P.; Zou, J.; Wu, Y.; Yu, C. α-MoO_3 Nanobelts: A High Performance Cathode Material for Lithium Ion Batteries. *J. Phys. Chem. C* **2010**, *114*, 21868–21872.

(29) Yu, M.; Shao, H.; Wang, G.; Yang, F.; Liang, C.; Rozier, P.; Wang, C.-Z.; Lu, X.; Simon, P.; Feng, X. Interlayer Gap Widened α-Phase Molybdenum Trioxide as High-Rate Anodes for Dual-Ion Intercalation Energy Storage Devices. *Nat. Commun.* **2020**, *11*, 1348.

(30) Brezesinski, T.; Wang, J.; Tolbert, S. H.; Dunn, B. Ordered Mesoporous α-MoO_3 with Iso-Oriented Nanocrystalline Walls for Thin-Film Pseudocapacitors. *Nat. Mater.* **2010**, *9*, 146–151.

(31) Kim, H.-S.; Cook, J. B.; Lin, H.; Ko, J. S.; Tolbert, S. H.; Ozolins, V.; Dunn, B. Oxygen Vacancies Enhance Pseudocapacitive Charge Storage Properties of MoO_{3-x}. *Nat. Mater.* **2017**, *16*, 454–460.

(32) Pistoia, G.; Temperoni, C.; Cignini, P.; Icovi, M.; Panero, S. Non-Stoichiometric Molybdenum Oxides as Cathodes for Lithium Cells: Part III. Cells Based on $Mo_{18}O_{52}$. *J. Electroanal. Chem.* **1980**, *108*, 169–180.

(33) Cignini, P.; Icovi, M.; Panero, S.; Pistoia, G.; Temperoni, C. Non-Stoichiometric Molybdenum Oxides as Cathodes for Lithium Cells: Part I. Primary Batteries. *J. Electroanal. Chem.* **1979**, *102*, 333–341.

(34) Christian, P. A.; Carides, J. N.; DiSalvo, F. J.; Waszczak, J. V. Molybdenum Oxide Cathodes in Secondary Lithium Cells. *J. Electrochem. Soc.* **1980**, *127*, 2315–2319.

(35) Zhang, C.; Gao, M. C.; Yang, Y.; Zhang, F. Thermodynamic Modeling and First-Principles Calculations of the Mo-O System. *CALPHAD* **2014**, *45*, 178–187.

(36) Greenblatt, M. Monophosphate Tungsten Bronzes. A New Family of Low-Dimensional, Charge-Density-Wave Oxides. *Acc. Chem. Res.* **1996**, *29*, 219–228.

(37) Magnéli, A. The Crystal Structure of Mo_4O_{11} (gamma-Molybdenum Oxide). *Acta Chem. Scand.* **1948**, *2*, 861–871.

(38) Åsbrink, S.; Kihlborg, L. A Study of the Crystal Symmetry and Structure of Orthorhombic Mo_4O_{11} by Least-Squares Techniques. *Acta Chem. Scand.* **1964**, *18*, 1571–1573.

(39) Fun, H.-K.; Yang, P.; Sasaki, M.; Inoue, M.; Kadomatsu, H. Rietveld Refinement of the Crystal Structure of γ-Mo_4O_{11}. *Powder Diffr.* **1999**, *14*, 284–288.

(40) Inzani, K.; Nematollahi, M.; Vullum-Bruer, F.; Grande, T.; Reenaas, T. W.; Selbach, S. M. Electronic Properties of Reduced Molybdenum Oxides. *Phys. Chem. Chem. Phys.* **2017**, *19*, 9232.

(41) Bursill, L. A. On the Relation Between Molybdenum Trioxide and Rhenium Trioxide Type Crystal Structures. *Acta Crystallogr.* **1973**, *A29*, 28–30.

(42) Momma, K.; Izumi, F. VESTA: a Three-dimensional Visualization System for Electronic and Structural Analysis. *J. Appl. Crystallogr.* **2008**, *41*, 653–658.

(43) Icovi, M.; Panero, S.; D'Agate, A.; Pistoia, G.; Temperoni, C. Non-Stoichiometric Molybdenum Oxides as Cathodes for Lithium Cells: Part II. Secondary Batteries. *J. Electroanal. Chem.* **1979**, *102*, 343–349.

(44) Sánchez, R. H.; Treviño, L.; Fuentes, A. F.; Martínez-de la Cruz, A.; Torres-Martínez, L. M. Electrochemical Lithium Insertion in Two Polymorphs of a Reduced Molybdenum Oxide (γ and γ'-Mo_4O_{11}). *J. Solid State Electrochem.* **2000**, *4*, 210–215.

(45) Andersson, G.; Magnéli, A. On the Crystal Structure of Molybdenum Trioxide. *Acta Chem. Scand.* **1950**, *4*, 793–797.

(46) Kihlborg, L. Studies on Molybdenum Oxides. *Acta Chem. Scand.* **1959**, *13*, 954–962.

(47) Coelho, A. A. TOPAS and TOPAS-Academic: an Optimization Program Integrating Computer Algebra and Crystallographic Objects Written in C++. *J. Appl. Crystallogr.* **2018**, *51*, 210–218.

(48) Kieffer, J.; Valls, V.; Blanc, N.; Hennig, C. New Tools for Calibrating Diffraction Setups. *J. Synchrotron Radiat.* **2020**, *27*, 558–566.

(49) Baltrusaitis, J.; Mendoza-Sanchez, B.; Fernandez, V.; Veenstra, R.; Dukstiene, N.; Roberts, A.; Fairley, N. Generalized Molybdenum Oxide Surface Chemical State XPS Determination via Informed Amorphous Sample Model. *Appl. Surf. Sci* **2015**, *326*, 151–161.

(50) Xu, C.; Sun, B.; Gustafsson, T.; Edström, K.; Brandell, D.; Hahlin, M. Interface Layer Formation in Solid Polymer Electrolyte Lithium Batteries: an XPS Study. *J. Mater. Chem. A* **2014**, *2*, 7256–7264.

(51) Choi, J.-G.; Thompson, L. T. XPS Study of As-Prepared and Reduced Molybdenum Oxides. *Appl. Surf. Sci.* **1996**, *93*, 143–149.

(52) Briggs, D.; Seah, M. P. *Practical Surface Analysis by Auger and X-ray Photoelectron Spectroscopy*; Wiley: New York, 1983.

(53) National Institute of Standards and Technology, NIST X-ray Photoelectron Spectroscopy Database. 2000.

(54) Spevack, P. A.; McIntyre, N. S. A Raman and XPS Investigation of Supported Molybdenum Oxide Thin Films. 1. Calcination and Reduction Studies. *J. Phys. Chem.* **1993**, *97*, 11020–11030.

(55) Baek, S. W.; Wyckoff, K. E.; Butts, D. M.; Bienz, J.; Likitchatchawankun, A.; Preefer, M. B.; Frajnkovič, M.; Dunn, B. S.; Seshadri, R.; Pilon, L. *Operando* Calorimetry Informs the Origin of Rapid Rate Performance in Microwave-Prepared $TiNb_2O_7$ Electrodes. *J. Power Sources* **2021**, *490*, 229537.

(56) Baek, S. W.; Preefer, M. B.; Saber, M.; Zhai, K.; Frajnkovič, M.; Zhou, Y.; Dunn, B. S.; der Ven, A. V.; Seshadri, R.; Pilon, L. Potentiometric Entropy and *Operando* Calorimetric Measurements Reveal Fast Charging Mechanisms in PNb_9O_{25}. *J. Power Sources* **2022**, *520*, 230776.

(57) Pasquali, M.; Pistoia, G.; Rodante, F. Non-Stoichiometric Molybdenum Oxides as Cathodes for Lithium Cells: Part V. Thermodynamic, Kinetic and Structural Aspects of the Behaviour of Mo_8O_{23} and $Mo_{18}O_{52}$. *Solid State Ion.* **1982**, *6*, 319–325.

(58) Barker, J.; Saidi, M. Y.; Swoyer, J. L. Synthesis and Electrochemical Insertion Properties of the Layered Li_xMoO_2 Phases ($x = 0.74$, 0.85, and 1.00). *Electrochem. Solid-State Lett.* **2003**, *6*, A252–A256.

(59) Gatehouse, B. M.; Lloyd, D. J. The Redetermination of the Crystal Structure of a Sodium Molybdenum Oxide Bronze: $Na_{0.9}Mo_6O_{17}$. *J. Chem. Soc. D* **1971**, 13.

(60) Eda, K.; Kunotani, F.; Uchiyama, N. Low-Temperature Synthetic Route Based on the Amorphous Nature of Giant Species for Preparation of Lower Valence Oxides. *J. Solid State Chem.* **2005**, *178*, 1471–1477.

(61) Ramanujachary, K. V.; Collins, B. T.; Greenblatt, M.; McNally, P.; McCarroll, W. H. Substitutional Effects on the Electrical Properties of the Purple Bronze $Li_{0.9}Mo_6O_{17}$. *Solid State Ion.* **1986**, *22*, 105–115.

(62) Onoda, M.; Toriumi, K.; Matsuda, Y.; Sato, M. Crystal Structure of Lithium Molybdenum Purple Bronze $Li_{0.9}Mo_6O_{17}$. *J. Solid State Chem.* **1987**, *66*, 163–170.

(63) Zoller, M.; Bubnova, R.; Biryukov, Y.; Haussühl, E.; Pöttgen, R.; Janka, O.; Penner, S.; Praty, C.; Fitzek, H.; Winkler, J.; Filatov, S.; Huppertz, H. Elucidating the Physical Properties of the Molybdenum Oxide Mo_4O_{11} and Its Tantalum Substituted Variant $Mo_2Ta_2O_{11}$. *Z. Für Krist. - Cryst. Mater.* **2020**, *235*, 143–155.

(64) Nazri, G.-A.; Julien, C. Far-Infrared and Raman Studies of Orthorhombic MoO_3 Single Crystal. *Solid State Ion.* **1992**, *53*, 376–382.

(65) Dieterle, M.; Mestl, G. Raman Spectroscopy of Molybdenum Oxides Part II. Resonance Raman Spectroscopic Characterization of the Molybdenum Oxides Mo_4O_{11} and MoO_2. *Phys. Chem. Chem. Phys.* **2002**, *4*, 822–826.

(66) Bashian, N. H.; Abdel-Latif, S.; Zuba, M.; Griffith, K. J.; Ganose, A. M.; Stiles, J. W.; Zhou, S.; Scanlon, D. O.; Piper, L. F. J.; Melot, B. C. Transition Metal Migration Can Facilitate Ionic Diffusion in Defect Garnet-Based Intercalation Electrodes. *ACS Energy Lett.* **2020**, *5*, 1448–1455.

(67) Otero, M.; Sigal, A.; Perassi, E.; Barraco, D.; Leiva, E. Statistical Mechanical Modeling of the Transition Stage II→Stage I of Li-Ion Storage in Graphite. A Priori vs Induced Heterogeneity. *Electrochim. Acta* **2017**, *245*, 569–574.

(68) Schlueter, S.; Genieser, R.; Richards, D.; Hoster, H. E.; Mercer, M. P. Quantifying Structure Dependent Responses in Li-Ion Cells with Excess Li Spinel Cathodes: Matching Voltage and Entropy Profiles Through Mean Field Models. *Phys. Chem. Chem. Phys.* **2018**, *20*, 21417–21429.

(69) Baek, S. W.; Saber, M.; der Ven, A. V.; Pilon, L. Thermodynamic Analysis and Interpretative Guide of Entropic Potential Measurements of Battery Electrodes. *J. Phys. Chem. C* **2022**, *126*, xxx–xxx, DOI: 10.1021/acs.jpcc.1c10414.

(70) Hudak, N. S.; Davis, L. E.; Nagasubramanian, G. Cycling-Induced Changes in the

Entropy Profiles of Lithium Cobalt Oxide Electrodes. *J. Electrochem. Soc.* **2015**, *162*, A315–A321.

Graphical TOC Entry

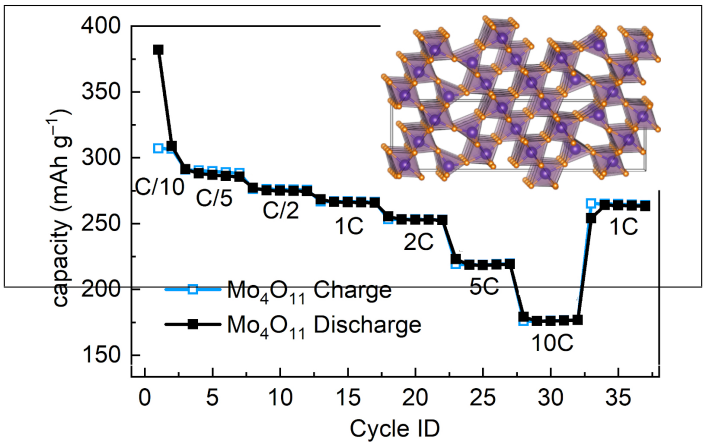

SI: High-Rate Lithium Cycling and Structure Evolution in Mo_4O_{11}

Rebecca C. Vincent,[†] Yunkai Luo,[‡] Jessica L. Andrews,[¶] Arava Zohar,[†] Yucheng Zhou,[§] Qizhang Yan,[∥] Eve M. Mozur,[†] Molleigh B. Preefer,[⊥] Johanna Nelson Weker,[⊥] Anthony K. Cheetham,[†] Jian Luo,[∥,#] Laurent Pilon,[§] Brent C. Melot,[¶,@] Bruce Dunn,[‡] and Ram Seshadri*[,†]

†*Materials Department and Materials Research Laboratory*
University of California, Santa Barbara, California 93106, United States
‡*Department of Materials Science and Engineering*
University of California, Los Angeles, California 90095, United States
¶*Department of Chemistry*
University of Southern California, Los Angeles, California 90089, United States
§*Mechanical and Aerospace Engineering Department*
University of California, Los Angeles, California 90095, United States
∥*Department of Nanoengineering*
University of California San Diego, La Jolla, California 92093, United States
⊥*Stanford Synchrotron Radiation Lightsource, SLAC National Accelerator Laboratory*
Menlo Park, California 94025, USA
#*Program of Materials Science and Engineering*
University of California San Diego, La Jolla, California 92093, United States
@*Department of Chemical Engineering and Materials Science, University of Southern California, Los Angeles, CA 90089, USA*

E-mail: seshadri@mrl.ucsb.edu

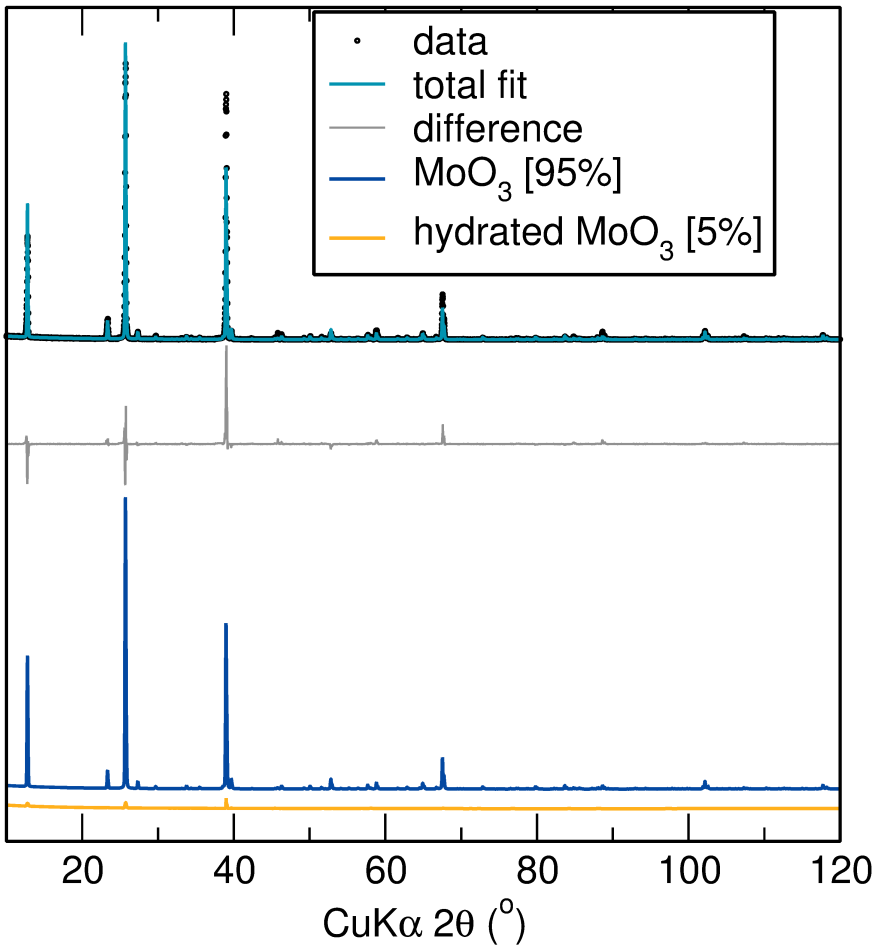

Figure S1: Rietveld refinement of the powder X-ray diffraction pattern of the dehydrated MoO_3, precursor to Mo_4O_{11}. Preferred orientation in the sample makes it more difficult to get a good fit of laboratory XRD data.

Table S1: Fit parameters for the Rietveld refinement of synchrotron diffraction data from Mo_4O_{11}.

Chemical formula	Mo_4O_{11}			
Space group	$Pna21$			
Unit cell dimensions				
a	24.4723(1) Å			
b	6.7512(1) Å			
c	5.4568(1) Å			
α	90°			
β	90°			
γ	90°			
Volume	901.56 Å^3			
site	x	y	z	B_{eq} (Å^2)
Mo1	0.0285	0.1590	0.5256	0.309
Mo2	-0.0874	0.5212	0.5239	0.247
Mo3	0.6469	0.6967	0.5303	0.163
Mo4	0.7945	0.8722	0.5123	0.031
O1	0.6926	0.4799	0.7289	0.860
O2	-0.0313	0.3449	0.5351	0.547
O3	-0.0032	-0.0064	0.2910	0.465
O4	0.7236	0.8221	0.5498	0.423
O5	0.0626	0.3149	0.2560	0.445
O6	0.6868	0.5421	0.2408	1.726
O7	0.8363	0.6554	0.5362	1.395
O8	0.8705	0.3267	0.2968	0.871
O9	0.0653	0.3406	0.7645	0.765
O10	0.8751	0.3561	0.8073	1.138
O11	0.0949	-0.0201	0.5305	1.048

Table S2: Bond Valence Sum analysis of the refined Mo_4O_{11} structure using $V = \sum_{v_i} \exp\{(R_0 - R_i)/b\}$ where V is the valence of an atom, a sum of the individual bond valences v_i, where R_i is the observed bond length, R_0 is the ideal bond length if the element i had a valence of exactly 1, and b is an empirical constant. Both R_0 and b are tabulated parameters – we referenced the list compiled by I. David Brown at McMaster University and used 1.88 Å for Mo (approximating Mo^{4+}, Mo^{5+}, and Mo^{6+} to be the same) with b = 0.37 Å. As a double check, the V values for each Mo add up to 22.03, which balances the charge from the 11 O^{-2} in the unit cell.

Bond	R_i (Å)	v_i
Mo1–O2	1.931	0.871
Mo1–O3	1.867	1.04
Mo1–O3	1.883	0.992
Mo1–O5	1.992	0.739
Mo1–O9	2.004	0.715
Mo1–O11	2.024	0.678
Mo1 $V = 5.03$		
Mo2–O2	1.817	1.19
Mo2–O8	2.079	0.584
Mo2–O10	2.116	0.528
Mo2–O9	1.779	1.31
Mo2–O5	1.788	1.28
Mo2–O7	2.076	0.589
Mo2 $V = 5.48$		
Mo3–O11	1.744	1.44
Mo3–O10	1.711	1.58
Mo3–O8	1.750	1.42
Mo3–O6	2.130	0.509
Mo3–O1	2.137	0.499
Mo3–O4	2.063	0.610
Mo3 $V = 6.06$		
Mo4–O1	1.738	1.47
Mo4–O6	1.756	1.40
Mo4–O4	1.778	1.32
Mo4–O7	1.791	1.27
Mo4 $V = 5.46$		

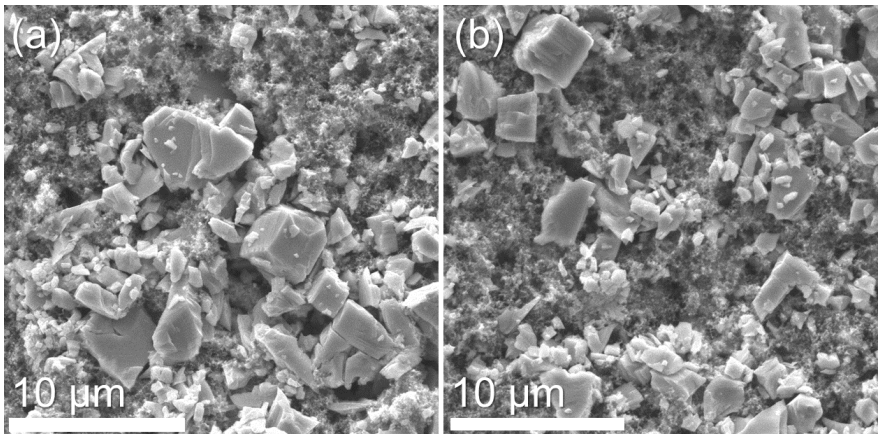

Figure S2: Two SEM images of the ball milled, slurry-cast Mo_4O_{11} electrode. Particles range in size from 1 to 5 μm.

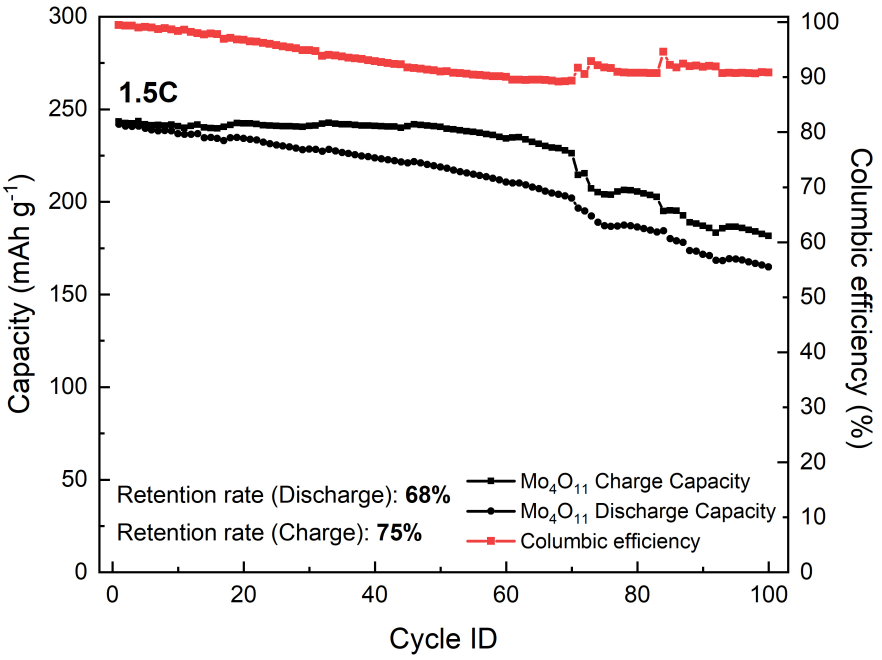

Figure S3: Long-term cycling of Mo_4O_{11} at a 1.5C rate between 1.2 V and 3.7 V.

Table S3: Analysis of the exponent b in the equation $i_p = av^b$ where i_p is the peak current and v is the voltage scan rate in variable rate CV of Mo_4O_{11} in the limited voltage range corresponding to Figure 3(a) in the manuscript.

Process	Voltage value of peak (*vs.* Li/Li^+ (V)	b
Oxidation	1.47	0.72
	1.89	0.66
	1.99	0.85
	2.34	0.92
	2.55	0.91
Reduction	1.43	0.71
	1.75	0.64
	1.94	0.85
	2.30	0.90
	2.44	0.91

Table S4: XPS fitting parameters for Mo_4O_{11} and the three *ex situ* samples.

Peak	Area	FWHM (eV)	Position (eV)
Uncycled Mo_4O_{11}			
Mo^{6+} $3d^{5/2}$	12404.9	1.45076	232.7539
Mo^{6+} $3d^{3/2}$	8269.9	1.45076	235.8717
Mo^{5+} $3d^{5/2}$	7614.3	1.39994	231.6003
Mo^{5+} $3d^{3/2}$	5076.2	1.39994	234.7283
Mo^{4+} $3d^{5/2}$	2011.8	1.12784	230.0051
Mo^{4+} $3d^{3/2}$	1341.2	1.12784	232.9651
Mo_4O_{11} discharged to 1.2 V 1 time			
Mo^{6+} $3d^{5/2}$	–	–	–
Mo^{6+} $3d^{3/2}$	–	–	–
Mo^{5+} $3d^{5/2}$	1587.0	2.23603	231.2703
Mo^{5+} $3d^{3/2}$	1058.0	2.23603	234.4705
Mo^{4+} $3d^{5/2}$	3669.3	1.76071	229.9225
Mo^{4+} $3d^{3/2}$	2446.2	1.76071	233.2067
Mo_4O_{11} discharged to 1.2 V, charged to 3 V			
Mo^{6+} $3d^{5/2}$	4865.0	1.22653	232.7747
Mo^{6+} $3d^{3/2}$	3243.3	1.22653	235.9350
Mo^{5+} $3d^{5/2}$	5960.2	1.85859	231.0467
Mo^{5+} $3d^{3/2}$	3973.4	1.85859	234.1806
Mo^{4+} $3d^{5/2}$	–	–	–
Mo^{4+} $3d^{3/2}$	–	–	–
Mo_4O_{11} discharged to 1.2 V 2 times			
Mo^{6+} $3d^{5/2}$	–	–	–
Mo^{6+} $3d^{3/2}$	–	–	–
Mo^{5+} $3d^{5/2}$	1417.3	2.49551	231.2547
Mo^{5+} $3d^{3/2}$	944.9	2.49551	234.3953
Mo^{4+} $3d^{5/2}$	3590.6	1.84114	229.8667
Mo^{4+} $3d^{3/2}$	2393.7	1.84114	233.1597

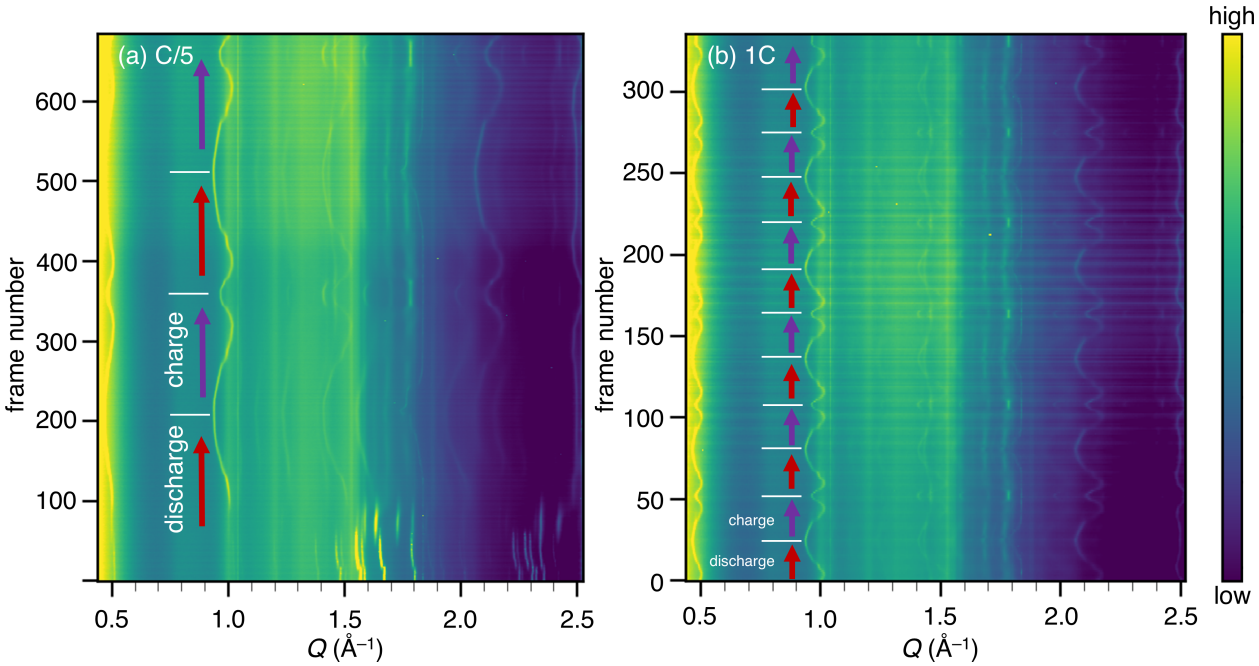

Figure S4: *Operando* synchrotron XRD of a Mo_4O_{11} cell cycling between 1.2 V and 3 V at (a) $C/5$ for over 2 full cycles before increasing the cycling rate in (b) to $1C$.